Development of a one-dimensional moving window atomistic framework to model steady state shock wave propagation

by

Alexander Davis

A thesis submitted to the Graduate Faculty of
Auburn University
in partial fulfillment of the
requirements for the Degree of
Master of Science

Auburn, Alabama
May 2, 2020

Keywords: shock waves, molecular dynamics, atomistic/continuum, multiscale modeling

Approved by

Vinamra Agrawal, Chair, Assistant Professor of Aerospace Engineering
Asha-Dee Celestine, Assistant Professor of Aerospace Engineering
Dudley Nichols, Assistant Professor of Aerospace Engineering
Pradeep Lall, John and MacFarlane Endowed Distinguished Professor Department of Mechanical Engineering
Andrew Adamczyk, Assistant Professor of Chemical Engineering
George Flowers, Dean of the Graduate School

Abstract

We develop a long-time, large-domain moving window atomistic framework using Molecular Dynamics (MD) to model shock wave propagation through a one-dimensional system. We implement ideas of control volume on a MD framework where a moving window follows a propagating shock. This circumvents issues such as boundary reflections and transient effects typically observed in conventional MD shock simulations. We model shock wave propagation through a one-dimensional chain of copper atoms using the Lennard-Jones, modified Morse, and Embedded Atom Model (EAM) interatomic potentials. The domain is divided into purely atomistic "window" atoms flanked by boundary, or continuum, atoms which incorporate either a Nose-Hoover or Langevin thermostat. The propagating shock wave is contained within the window region, while continuum shock conditions are imposed on the boundary atoms. The moving window effect is achieved by adding/removing atoms to/from the window and boundary regions. We perform verification studies to ensure proper implementation of the thermostats, potential functions, and moving window respectively. We then track the propagating shock and compare the actual shock velocity and average particle velocity to their corresponding input values. From these comparisons, we make corrections to the linear shock Hugoniot relation for the developed one-dimensional framework. Finally, we perform one-dimensional moving window simulations of a propagating stable-structured shock up to a few nanoseconds.

Acknowledgments

This thesis would not have been possible without the support and intellectual contributions of my advisor Dr. Vinamra Agrawal, whose excellent guidance and persistent encouragement during my time so far at Auburn have contributed greatly to my research interests as well as my professional development. I would like to thank my thesis committee for their valuable inputs in this research effort: Dr. Asha-Dee Celestine, Dr. Stephen Nichols, Dr. Pradeep Lall, and Dr. Andrew Adamczyk. I also thank Dr. Kaushik Bhattacharya for providing valuable discussion during the development of the framework. Additionally, I thank my parents and siblings whose love and support I will never be able to fully repay. Most of all, I thank my wife Olivia for her patience and unceasing love throughout our journey so far.

This thesis is based upon work supported financially by the US Department of Defense through the National Defense Science and Engineering Graduate (NDSEG) Fellowship Program. Simulations were performed using Hopper computing cluster at Auburn University.

Table of Contents

List of Figures

Chapter 1

Introduction

The propagation of shock waves in materials is an important scientific phenomenon that has been studied extensively for many decades; see, for example, [1, 2] and the references therein. A shock is defined as a moving wave front or disturbance which suffers discontinuities in stress, strain, particle velocity, and temperature across the wave boundary. These four parameters along with the shock wave velocity constitute the five primary values necessary to describe the motion of a shock wave through a material. These parameters can be obtained through the jump conditions derived from the equations of conservation of mass and momentum, a thermodynamic relationship derived from the shock Hugoniot/release isentrope, and a constitutive relation, referred to here as an Equation of State (EOS). Typically shock waves occur in a material under high strain rate loading conditions such as high speed impact.

Shock waves, by their very nature, are a three-dimensional, macro-scale occurrence. Because of this, much of the research conducted on shock compression/propagation in solids has focused on the macroscopic level. Refer to [3, 4, 5, 6, 7, 8] for reviews of high-stress shock compression in solids as well as experimental approaches to the problem of calculating the stress-compression states behind these shocks. However, the shock response of a material at any length scale is inextricably linked to its response at lower length scales. At the macroscopic scale, shock waves can lead to damage, plastic deformation, and fracture of the material. At the micro- and meso-scale, shock waves can interact with the microstructure resulting in complex behavior such as scattering, grain rotations, pore collapse, phase transformations, dislocation and void generation, and grain crushing [9, 10, 11].

Because of this connection between the different length scales, there has been growing interest in the past several decades in modeling shock propagation at the microscopic scale using Molecular Dynamics (MD) techniques. One of the first works to do this was [12]. In this paper, Paskin and Dienes simulated a shock wave moving through a three-dimensional Lennard-Jones solid using MD techniques. They found that the values for stress and strain calculated from MD were in agreement with the values derived from the Hugoniot relations. Additionally, they saw a large temperature increase behind the shock wave which they attributed to kinetic energy transfer by direct collisions with atoms at the shock wave front. This work established the value of using MD to model shock waves in high-stress regimes.

Paskin and Dienes then produced a series of papers [13, 14, 15] expanding on their newly-developed MD framework. Specifically, [15] showed that the average shock temperature derived from the Hugoniot conservation relations and the Mie-Gruneisen EOS was in good agreement with the average shock temperature obtained from MD for face-centered cubic (FCC) and body-centered cubic (BCC) solids. In [16, 17, 18, 19], Tsai and MacDonald also studied shock propagation in three-dimensional crystalline latices by means of MD simulations. Hardy built off these works in [20] by deriving formulas to relate local continuum properties such as mass density, momentum density, etc. to the masses, positions, and velocities of the particles whose motion was simulated with MD. These formulas were similar to those presented in [21] but had forms which could be easily implemented in MD simulations.

More recent research has used these classic works to model the shock response of materials using purely atomsitic methods [22, 23, 24, 25]. These simulations typically involve a large number of atoms ($\sim O(10^5 - 10^9)$) subjected to flyer-plate loading scenarios. Such simulations have been used to study void nucleation, dislocation generation [26], twinning [27] and even shock induced spallation [10, 25, 28]. However, purely atomistic methods suffer from domain boundary effects and unwanted wave reflections from boundaries. Additionally, purely atomistic shock simulations typically lead to unrealistic strain rates $(10^{10} - 10^{12} s^{-1})$ [1]. Such strain rates are rare and orders of magnitude higher than those observed in experiments and practical scenarios $(10^6 - 10^8 s^{-1})$. From a purely atomistic perspective, the multiscale shock technique

(MSST), which has been developed in the past decade [29], performs long-time shock simulations on a small atomistic domain for a much lower computational cost than conventional MD simulations. MSST also allows for multiple shock waves. While this technique permits the shock to be controlled based on prescribed continuum constraints, it does not allow the information to communicate from atomistic to continuum and back.

Concurrent multiscale methods have been developed in the past few decades where the domain is divided into a coarse-scaled (continuum) region and a fine-scaled (atomistic) region [30, 31]. Such concurrent multiscale methods can be classified into two sub-categories: hierarchical and domain decomposition. Hierarchical methods use all length scales at every point in the domain, i.e. the coarse-scale model receives information from the fine-scale model to develop a constitutive law while the fine-scale model receives information from the coarse-scale model about the boundary conditions [30]. On the other hand, domain decomposition methods divide the problem into non-overlapping, contiguous domains which evolve concurrently in time. In most concurrent atomistic/continuum domain decomposition methods, atomsitic domains are employed where nanoscale structures and phenomena are described [32]. The atoms in these domains are updated using standard atomistic methods such as MD, and the atomistic domain is typically the 'region of interest' where information from lower length scales is needed.

[33] first verified an atomistic/continuum multiscale modeling method by creating an atomistic core with a surrounding continuum region and describing the domain in terms of non-local elasticity theory. The framework was verified using static and dynamic tests, and it was applied to crack propagation on cleavage and non-cleavage planes in BCC crystals. Numerous approaches have since been developed to combine the atomistic domain (for describing short-range dislocation cores) with the continuum domain (for addressing long-range dislocation elastic fields). Over the past 17 years, many reviews have compared the theoretical foundations of these various multiscale methods [34, 35, 36, 37, 38, 39, 40], and [41] implemented 14 atomistic/continuum coupling techniques to simulate a Lomer dislocation dipole. For an in-depth and comprehensive review of the literature applying 'atomistic/continuum' approaches to MD over the past three decades, refer to [42].

In developing concurrent multiscale methods, it is imperative to ensure the compatibility of the interface region between fine-scaled and coarse-scaled regions. Despite tremendous advances in recent years, issues which are inherent with atomistics, such as uncertainty in the interatomic potential and high strain rates in MD, remain with concurrent atomistic/continuum (A/C) methods. Moreover, this approach introduces an additional source of error associated with the domain interface, across which there is a discrepancy in material description, governing equations, and numerical resolution. As expounded upon in [42], this discrepancy creates spurious wave reflections at the domain interface. One reason for these transient effects is the fact that differences in vibrational properties between the two domains lead to aphysical scattering at the atomistic/continuum interface [43]. Additionally, the continuum domain typically has a larger characteristic element length and hence a lower numerical resolution. Therefore, this domain may not receive all of the wave information from the atomistic domain, which typically has a finer resolution and permits shorter wavelengths.

Recently, much work has been done to improve the absorption of energetic pulses impinging on the A/C interfaces and thus reduce the number of phonon reflections into the atomistic domain. For example, [44] developed a time-dependent boundary condition coupling the atomistic region to linear surroundings while [45] introduced a new class of matching conditions between the two domains. Additionally, [46] inserted a supplementary damping term into the Langevin equations of motion for atoms in a 'stadium' boundary region near the interface. Also, [47] presented the application of digital filters to selectively damp the kinetic energy of the atoms in the atomistic domain. Some other existing concurrent schemes such as the quasi-continuum (QC) method [48, 49, 50, 51] and coupled atomistic discrete dislocation (CADD) method [52, 53, 54, 55] attempt to remedy the issues associated with the A/C interface by implementing a pad region which acts as a boundary condition for both atomistic and continuum regions.

While existing concurrent schemes have been very successful in modeling material defects and their motion, they have not been extended to model shock wave propagation through a material. To model shock wave propagation using concurrent multiscale schemes, the atomistic region of interest must move along with the shock. This motion of the atomistic region requires

simultaneous refinement of the continuum region as well as coarsening of the atomistic region at the speed at which the shock wave is moving. At the same time, the scattered elastic waves and resulting microstructural defects must consistently cross the interface to the continuum region. Additionally, material behavior under shock loading is governed by a highly nonlinear equation of state adding more complications into the formulation.

In the present work, we use ideas of control volume to develop a long-time, large-domain moving window atomistic framework to model shock wave propagation through a one-dimensional chain of copper atoms. The formulation is inspired from [56] and the supplemental material of [57]. The domain is divided into an inner 'window' region containing the shock wave flanked by a 'boundary' region on both sides. The atoms in the boundary region are governed by continuum shock equations and act as boundary conditions for the window region. The motion of the window region is achieved by consistently adding and removing atoms to and from the boundary and window regions. The framework, in its current state, is not a truly concurrent atomistic/continuum scheme in that it lacks a continuum region with finite element type mesh points. The scope of this work is therefore limited to ensuring that the formulation can follow a shock wave for a long time without artificial wave generation and reflection.

In addition to developing the moving window atomistic method for use in shock propagation modeling, the present paper also utilizes this method to calculate a relation between the particle velocity and shock wave velocity in one dimension. Much work has been done using shock propagation to study the dynamic properties of a variety of different materials subject to compression. For a summary of the data from many of these experiments, see [58]. For many of the materials included in these studies, a linear relation has been found between the shock wave velocity and particle velocity over a large range of the data. This linear relation has been used extensively in the shock literature; see, for example, [59, 60, 61, 62] and their associated references.

Other experiments have performed theoretical investigations into the origins of the shock kinetic relation. For example, [63] supplemented the shock EOS with a kinetic relation that relates the shock front's dissipation rate to the shock velocity. Previously, [64, 65] introduced this framework in the context of phase transitions, but [63] showed that it also applied in the study

of shocks. [66] utilized this framework to analyze a plate impact-induced shock wave propagation through a one-dimensional medium. However, the numerical methods they employed had limited resolution which became problematic when introducing multiple reflections. Research is ongoing in the development of computational methods to understand the relation between the linear shock wave parameters from an atomistic standpoint. The present paper starts with the experimentally known linear law for copper and performs steady state simulations using shock speeds obtained from the known kinetic relation. Next, the paper provides corrections to the linear law for a one-dimensional case to ensure steady shock speed.

The paper is organized as follows. Chapter 2 outlines a classic shock Riemann problem of a single propgating shock wave with constant states across it. Chapters 3 and 4 describe the one-dimensional framework and its components, including thermostats, potentials, integration algorithms, and the moving window. Chapter 5 presents detailed verifications of every component of the framework. Finally, Chapter 6 presents results from the moving window atomistic framework including steady state shock simulations, calculations of a new equation of state in a one-dimensional setting, and effects of domain size.

Chapter 2

Governing Equations

We study shock wave propagation through an idealized, one-dimensional chain of copper (Cu) atoms along the close packed $[110]$ direction. In a three-dimensional sense, this case corresponds to a planar shock propagating along the close packed direction. For the purpose of simplicity, shock induced plastic effects, defect generation and phase transformations are ignored in this work.

Consider the case of a shock passing through a body Ω. We assume that the boundary of

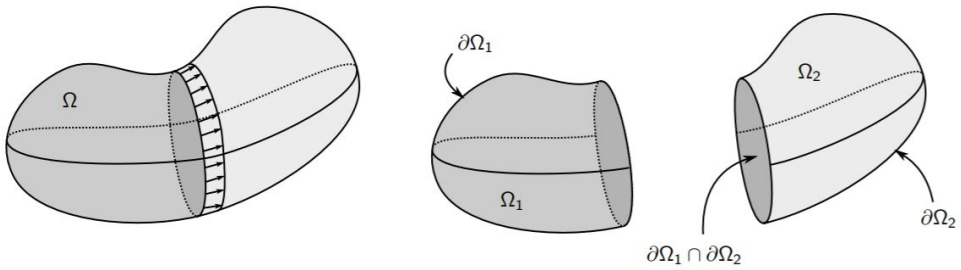

Figure 2.1: Discontinuous wave propagating through a three-dimensional material.

the shock wave front is contained within the boundary of the material. This creates a partitioning $\Omega = \Omega_1 \cap \Omega_2$ of the body into two regions on either side of the discontinuity, where the displacements are continuous.

2.1 Continuity jump condition

Consider a point $\mathbf{s}$ on the discontinuity which moves with the discontinuity in time. Here, $\dot{\mathbf{s}}$ is the velocity of the discontinuity at the point $\mathbf{s}$. The material neither creates a void nor

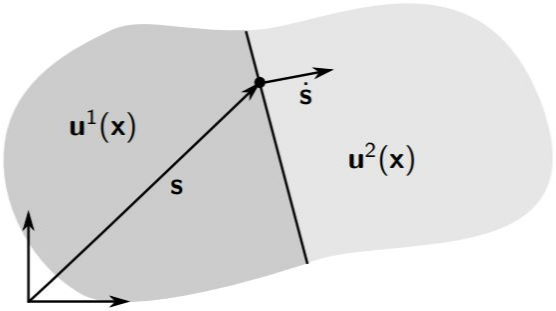

Figure 2.2: Point $\mathbf{s}$ on discontinuity propagating through material with velocity $\dot{\mathbf{s}}$.

interpenetrates itself, so the displacement is continuous at $\mathbf{s}(t)$ for all time:

$$\mathbf{u}^1(\mathbf{s}, t) = \mathbf{u}^2(\mathbf{s}, t). \tag{2.1}$$

Taking the total derivative of each side with respect to time and using index notation, we get the following:

$$\begin{aligned} \frac{d}{dt} u_i^1(\mathbf{s}(t), t) &= \frac{d}{dt} u_i^2(\mathbf{s}(t), t) \\ \frac{\partial u_i^1}{\partial s_j} \frac{ds_j}{dt} + \frac{\partial u_i^1}{\partial t} &= \frac{\partial u_i^2}{\partial s_j} \frac{ds_j}{dt} + \frac{\partial u_i^2}{\partial t} \\ \epsilon_{ij}^1 \dot{s}_j + v_i^1 &= \epsilon_{ij}^2 \dot{s}_j + v_i^2 \end{aligned} \tag{2.2}$$

where ϵ and v denote strain and particle velocity respectively. We adopt the notation $[\![\cdot]\!]$ to denote the change in a quantity across the shock. Then, we can write Eq. (2.2) as

$$[\![\epsilon]\!]\dot{\mathbf{s}} + [\![\mathbf{v}]\!] = 0. \tag{2.3}$$

2.2 Momentum jump condition

The integral of the total force ($\mathbf{t} = \sigma\mathbf{n}$) over the boundary of the body equals the time derivative of the total momentum of the body,

$$\int_{\partial\Omega} \sigma \cdot \mathbf{n} dA = \frac{d}{dt} \int_{\Omega} \rho \mathbf{v} dV. \tag{2.4}$$

For the left hand side of the equation, we apply the divergence theorem to the two sub-bodies on either side of the discontinuity. Using index notation, we get the following:

$$\begin{aligned}
\int_\Omega \sigma_{ij,j} dV &= \int_{\Omega_1} \sigma_{ij,j} dV + \int_{\Omega_2} \sigma_{ij,j} dV \\
&= \int_{\partial\Omega} \sigma_{ij} n_j dA + \int_{\partial\Omega_1 \cap \partial\Omega_2} \sigma^1_{ij,j} n^1_j dA + \int_{\partial\Omega_1 \cap \partial\Omega_2} \sigma^2_{ij,j} n^2_j dA \\
&= \int_{\partial\Omega} \sigma_{ij} n_j dA + \int_{\partial\Omega_1 \cap \partial\Omega_2} [\![\sigma_{ij,j}]\!] n_j dA \\
\int_{\partial\Omega} \sigma_{ij} n_j dA &= \int_\Omega \sigma_{ij,j} dV - \int_{\partial\Omega_1 \cap \partial\Omega_2} [\![\sigma_{ij,j}]\!] n_j dA
\end{aligned} \tag{2.5}$$

where $\sigma_{ij,j} = \text{div}(\sigma)$. Next, we apply Reynold's transport theorem to the right-hand side of Eq. (2.4) to get

$$\frac{d}{dt} \int_{\Omega_1} \rho v_i dV = \int_{\Omega_1} \frac{\partial}{\partial t} \rho v_i dV + \int_{\partial\Omega_1} \rho v_i \dot{s}_j n_j dA \tag{2.6}$$

where $\dot{\mathbf{s}}$ is the boundary velocity. Thus, we can write

$$\begin{aligned}
\frac{d}{dt} \int_\Omega \rho v_i dV &= \int_\Omega \frac{\partial}{\partial t} \rho v_i dV + \int_{\partial\Omega_1} \rho^1 v^1_i \dot{s}_j n^1_j dA + \int_{\partial\Omega_2} \rho^2 v^2_i \dot{s}_j n^2_j dA \\
&= \int_\Omega \frac{\partial}{\partial t} \rho v_i dV + \int_{\partial\Omega_1 \cap \partial\Omega_2} [\![\rho v_i]\!] \dot{s}_j n_j dA.
\end{aligned} \tag{2.7}$$

Combining Eqs. (2.5) and (2.7), we get the following:

$$\int_\Omega \sigma_{ij,j} dV - \int_{\partial\Omega_1 \cap \partial\Omega_2} [\![\sigma_{ij,j}]\!] n_j dA = \int_\Omega \frac{\partial}{\partial t} \rho v_i dV + \int_{\partial\Omega_1 \cap \partial\Omega_2} [\![\rho v_i]\!] \dot{s}_j n_j dA \tag{2.8}$$

which we can rewrite as

$$\int_\Omega \left[\sigma_{ij,j} - \frac{\partial}{\partial t} \rho v_i \right] dV = \int_{\partial\Omega_1 \cap \partial\Omega_2} \left([\![\sigma_{ij,j}]\!] + [\![\rho v_i]\!] \dot{s}_j \right) n_j dA. \tag{2.9}$$

Eq. (2.9) is true for *all* subregions of Ω, and it must hold true for all $\Omega \subset (\Omega_1 \cup \Omega_2)$. This only occurs if the integrand is zero. Then, the right hand side must hold for all subsets of the

boundary. By the fundamental lemma, we have the following jump condition:

$$[\![\sigma]\!]\mathbf{n} + [\![\rho\mathbf{v}]\!](\dot{\mathbf{s}} \cdot \mathbf{n}) = 0 \tag{2.10}$$

2.3 One-dimensional formulation

Consider the propagation of a discontinuity in a plane-strain or plane-stress material as shown in Fig. 2.3. In this case, we let the propagation of the discontinuity $\dot{\mathbf{s}} = \mathrm{U}_S$ be in the x_1 direction

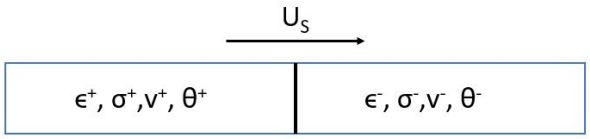

Figure 2.3: Discontinuous wave propagating through a one-dimensional material.

only. Substituting this into Eq. (2.3), we get the one-dimensional continuity jump condition in the Lagrangian frame,

$$[\![\epsilon]\!]U_S + [\![v]\!] = 0 \tag{2.11}$$

where ϵ is the longitudinal strain and $\mathbf{v}$ is the particle velocity. Next, substituting into Eq. (2.10), we get the one-dimensional momentum jump condition in the Lagrangian frame,

$$[\![\sigma]\!] + \rho U_S[\![v]\!] = 0 \tag{2.12}$$

where σ is the longitudinal stress. Here, we assume that the wave does not significantly affect the material properties, so $\rho^+ = \rho^- = \rho$.

The shock jump equations are supplemented by an empirically observed linear relation between shock speed and particle velocity,

$$U_s = C_0 + S[\![v]\!]. \tag{2.13}$$

Here, *S* is a dimensionless, empirical parameter (1.49 for Cu [58]) and C_0 is the sound velocity in the material at zero stress (39.4 for Cu [1]). Equation (2.13) was first presented in [3] and used to fit data for 23 metals. However, [58] tabulated Hugoniot data which offered linear

fits for many different types of materials. In some cases – for example, materials with phase transitions, porosity, or molecular bonding – the linear relation can break down [67]. However, even in those instances, the linear relation is still used, at least for representing the data over part of the range. Equations (2.11), (2.12), and (2.13) lead to the standard Hugoniot stress-strain relationship as

$$\sigma = \frac{\rho C_0 \epsilon}{(1 - S\epsilon)^2} \tag{2.14}$$

where compression strain is considered positive. The Hugoniot stress-strain relationship forms the basis of modern equations of state (EOS). In this work, we use the Hugoniot EOS (2.14) for sake of simplicity and to quickly compute shocked states.

2.4 Temperature rise

As a shock wave moves through a solid, the material behind the wave front gets compressed, and thus the temperature rises. We assume the thermodynamic process at the shock front to be adiabatic and the release from the shock state to the initial state to be isentropic. For solid materials, the release isentrope and shock Hugoniot are nearly the same. Figure 2.4 [1] shows a material shocked from an initial state at atmospheric pressure to pressure P_1. Points P_1 and V_1

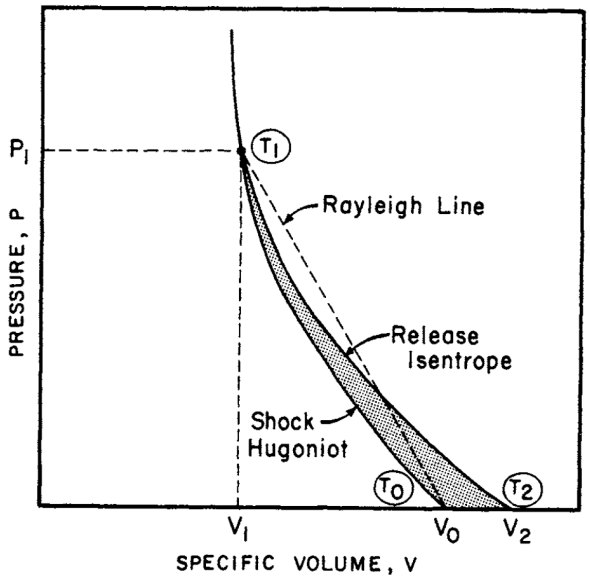

Figure 2.4: Shock Hugoniot and release isentrope leading to temperatures T_1 and T_2.

are on the shock Hugoniot, and unloading follows the release isentrope to point 2. It is apparent

that T_2 is higher than T_0, and thus V_2 is higher than V_0. This irreversibility produces a loss of energy as shown by the grey area. We can calculate the rise in temperature behind the shock using the Grüneisen EOS and thermodynamic relationships.

Using the first law of thermodynamics

$$dE = \delta Q - \delta W \tag{2.15}$$

where

$$\delta W = PdV \tag{2.16}$$

and

$$\delta Q = TdS, \tag{2.17}$$

we obtain the new expression for the first law of thermodynamics:

$$dE = TdS - PdV. \tag{2.18}$$

We can use this to calculate a thermodynamic expression for TdS:

$$\begin{aligned} S &= f(T, V) \\ dS &= \left(\frac{\partial S}{\partial T}\right)_V dT + \left(\frac{\partial S}{\partial V}\right)_T dV \\ TdS &= T\left(\frac{\partial S}{\partial T}\right)_V dT + T\left(\frac{\partial S}{\partial V}\right)_T dV, \end{aligned} \tag{2.19}$$

where we know that

$$C_V = \left(\frac{\partial E}{\partial T}\right)_V = T\left(\frac{\partial S}{\partial T}\right)_V \tag{2.20}$$

is the volumetric specific heat capacity. Then, from the second Maxwell relation

$$dA = -PdV - SdT,$$

we get the following:

$$\left(\frac{\partial P}{\partial T}\right)_V = \left(\frac{\partial S}{\partial V}\right)_T. \tag{2.21}$$

Substituting (2.20) and (2.21) into (2.19) gives

$$TdS = C_V dT + T\left(\frac{\partial P}{\partial T}\right) dV. \tag{2.22}$$

We now apply the Grüneisen equation

$$\frac{\gamma}{V} = \left(\frac{\partial P}{\partial E}\right)_V$$

to get the following identity:

$$\left(\frac{\partial P}{\partial T}\right)_V = \left(\frac{\partial P}{\partial E}\right)_V \left(\frac{\partial E}{\partial T}\right)_V = \frac{\gamma}{V} C_V \tag{2.23}$$

where γ is the Mie-Grüneisen parameter for the material (2.0 for Cu [1]). Next, we substitute (2.22) and (2.23) into (2.18),

$$dE = C_V dT + T\frac{\gamma}{V} C_V dV - PdV. \tag{2.24}$$

For a Hugoniot shock process, we know that

$$\Delta E = (E_1 - E_0) = \frac{1}{2}(P_1 + P_0)(V_0 - V_1). \tag{2.25}$$

Expressing the change in internal energy with volume along the Hugoniot, we get the following for Eqs. (2.24) and (2.25):

$$\left(\frac{dE}{dV}\right)_H = C_V \left(\frac{dT}{dV}\right)_H + \frac{\gamma T}{V} C_V - P \tag{2.26}$$

$$\left(\frac{dE}{dV}\right)_H = \frac{1}{2}\left(\frac{dP}{dV}\right)_H (V_0 - V) - \frac{P}{2}. \tag{2.27}$$

Substituting (2.27) into (2.26), we get an equation for T,

$$C_V \left(\frac{dT}{dV}\right)_H + \frac{\gamma T C_V}{V} = \frac{1}{2}\left(\frac{dP}{dV}\right)_H (V_0 - V) + \frac{P}{2} \tag{2.28}$$

which is a differential equation of the form $Ay' + By = F(V)$. Writing Eq. (2.28) in terms of ϵ and σ, we arrive at our shock heat equation:

$$C_V \left(\frac{dT}{d\epsilon}\right)_H - \frac{\gamma T C_V}{1-\epsilon} = \frac{\epsilon}{2}\left(\frac{d\sigma}{d\epsilon}\right)_H - \frac{\sigma}{2}. \tag{2.29}$$

We can use this equation to solve for the jump in temperature across the shock wave front.

2.5 Problem statement

The state of the material is described by the state variables (v, ϵ, θ) on either side of the shock. Given a shock speed U_s and state $(v^-, \epsilon^-, \theta^-)$ of the unshocked material, equations (2.11), (2.12), (2.14), and (2.29) can be used to compute the state $(v^+, \epsilon^+, \theta^+)$ and stress σ of the shocked material. In this paper, we present a moving window framework to simulate long-time, steady state shock wave propagation using atomistics given continuum shock states ahead of and behind the shock. We study a classic Riemann problem of a single shock wave with constant states on either side as shown in Fig. 2.5.

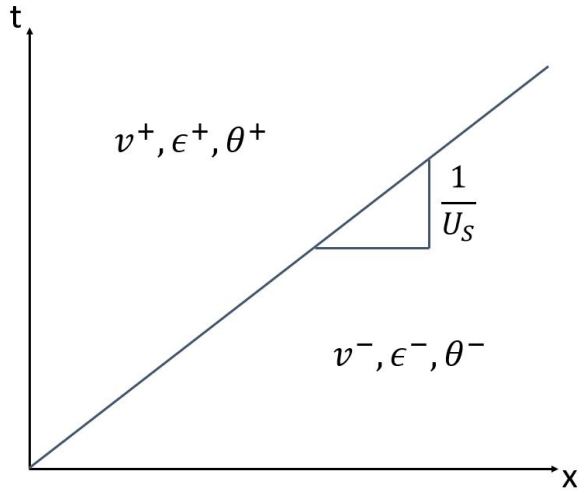

Figure 2.5: Riemann problem of a shock wave with constant states ahead of and behind the shock front.

Chapter 3

Development of the Atomistic Framework

The one-dimensional framework is implemented using an in-house C++ code. A chain of N Cu atoms of mass $m = 63.55$ amu is chosen, with x_i denoting the instantaneous position of the i^{th} atom at time t.

3.1 Geometry and boundary conditions

The atomistic chain is split into three sections as illustrated in Fig. 3.1. The outer atoms (in blue) are called *continuum* atoms (CA) while the inner atoms containing the shock wave front (SWF) are named *window* atoms (WA). The continuum Reimann states (v, ϵ, θ) are imposed on the CA region using standard algorithms for applying strain, mean particle velocity, and temperature (thermostats) [30]. The WA region is governed by classic MD equations. To ensure semi-infinite regions on either side of the shock wave, a semi-periodic boundary condition method is employed. To achieve this, the continuum atoms at the ends of the chain (x_0 and x_F) are made neighbors with the continuum atoms at the atomistic/continuum (A/C) interfaces ($x_{WA,0}$ and $x_{WA,F}$ respectively). The continuum atoms and window atoms near the A/C interfaces interact with each other. A two-dimensional representation of the A/C framework can be seen in Fig. 3.1.

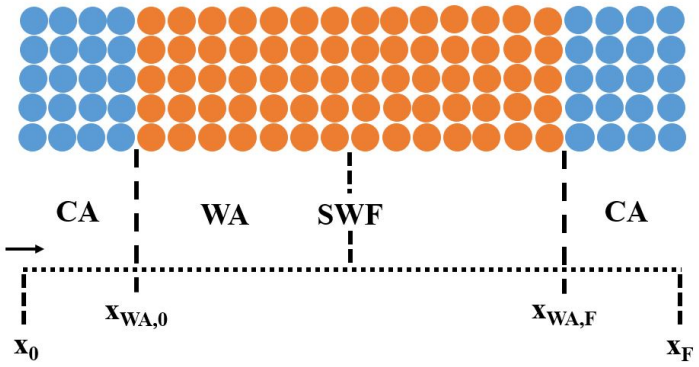

Figure 3.1: Schematic of the A/C framework.

3.2 Integration algorithm

To integrate the MD equations of motion, we utilize the widely-used velocity Verlet algorithm [68] as seen below:

$$\begin{aligned} x_i\left(t+\delta t\right) &= x_i\left(t\right) + v_i\left(t\right)\delta t + \frac{f_i\left(t\right)}{2m}\delta t^2 \\ v_i\left(t+\frac{\delta t}{2}\right) &= v_i\left(t\right) + \frac{\delta t}{2}\frac{f_i\left(t\right)}{m} \\ f_i\left(t+\delta t\right) &= f_i\left(x_i\left(t+\delta t\right)\right) \\ v_i\left(t+\delta t\right) &= v_i\left(t+\frac{\delta t}{2}\right) + \frac{\delta t}{2}\frac{f_i\left(t+\delta t\right)}{m} \end{aligned} \tag{3.1}$$

where x_i, v_i, and f_i denote the position of the i^{th} particle, its velocity, and the net force acting on it. The time step used in the integration algorithm is chosen to be $\delta t = 0.001$ ps.

3.3 Interatomic potentials

The temporal evolution of a window atom is described by Newton's 1D equations of motion, characteristic of the NVT ensemble, namely

$$m\frac{d^2x_i}{dt^2} = -\frac{\partial V_{TOT}}{\partial x_i}, \tag{3.2}$$

where $V_{TOT} = \sum_{i=1}^{N} V_i$ is the total potential energy of the entire system. Here, energy of i^{th} atom is calculated using $V_i = \sum_{j \in \{\text{neighbors}\}} V(x_{ij})$, where $V(x_{ij})$ is the interatomic potential which depends on the interatomic separation between atoms *i* and *j*: $x_{ij} = |x_i - x_j|$.

In this work, we utilize three different interatomic potential functions: Lennard-Jones (LJ), modified Morse, and Embedded Atom Model (EAM). The LJ potential only considers nearest-neighbor interactions and is represented most commonly as [69, 70]

$$V(x_{ij}) = 4\epsilon \left[\left(\frac{\sigma}{x_{ij}} \right)^{12} - \left(\frac{\sigma}{x_{ij}} \right)^{6} \right] = \epsilon \left[\left(\frac{x_0}{x_{ij}} \right)^{12} - 2 \left(\frac{x_0}{x_{ij}} \right)^{6} \right] \tag{3.3}$$

where ϵ is the depth of the potential well, σ is the finite distance at which the inter-particle potential is zero, and x_0 is the distance at which the potential reaches the minimum. The parameters for Cu are given by $\epsilon = 0.4093\ eV$ and $\sigma = 2.338\ \mathring{A}$ [71].

Like LJ, the modified Morse potential [72, 73] only considers nearest neighbor interactions. The expression is given by

$$V(x_{ij}) = \frac{D_0}{2B - 1} \left[e^{-2A\sqrt{B}(x_{ij} - x_0)} - 2Be^{-A(x_{ij} - x_0)/\sqrt{B}} \right]. \tag{3.4}$$

Here, we use the following parameters for Cu: $x_0 = 2.5471\ \mathring{A}$, $A = 1.1857\ \mathring{A}^{-1}$, $D_0 = 0.5869\ eV$, and $B = 2.265$ [73]. MacDonald and MacDonald [72] modified the standard Morse potential to improve the agreement with experimental values for the thermal expansion of copper [73].

Finally, the Embedded Atom Model (EAM) potential [74], is given by the expression

$$V(x_{ij}) = F\left(\sum_{i \neq j} \rho\left(x_{ij}\right) \right) + \frac{1}{2} \sum_{i \neq j} \phi\left(x_{ij}\right). \tag{3.5}$$

In this case, the total energy of a particular atom is a function of all the atoms within a cutoff radius $r_c = 5.507\ \mathring{A}$. Here, ϕ is a pair-wise potential function, ρ is the contribution to the electron charge density from atom *j* at the location of atom *i*, and *F* is an embedding function that represents the energy required to place atom *i* into the electron cloud [75]. As shown in [76], the EAM potential works very well for purely metallic systems with no directional

bonding and thus provides a robust means of calculating approximate structure and energetics of materials. In our case, we use the EAM potential file produced by [77].

3.4 Thermostats

The continuum atoms are subjected to continuum states $(v^+, \epsilon^+, \theta^+)$ and $(v^-, \epsilon^-, \theta^-)$. Temperatures θ^+ and θ^- are imposed using thermostatting algorithms. Two well-known examples of very distinct thermostats are considered in this paper: the Langevin thermostat [78, 79], and the Nose-Hoover thermostat [78, 80, 81]. As with many other thermostats, both the Langevin and Nose-Hoover thermostat are designed to maintain a system at thermal equilibrium for constant temperature MD simulations.

3.4.1 Langevin thermostat and stadium damping

The Langevin thermostat is a stochastic thermostat which adds a random force to the particle motion along with a damping term, ζ, which is introduced through fiction. Physically, this dissipative force term arises from fluctuating forces on a moving particle due to the chaotic motion of solvent molecules. The random force term is included to account for these fluctuating forces. The one-dimensional equations of motion of the Langevin thermostat for a particle *i* are as follows:

$$\begin{aligned} f_i^{tot}(t) &= f_i(t) - \zeta m_i v_i(t) + \sqrt{\frac{2k_B T \zeta m}{\delta t}} \tilde{h}_i(t) \\ \left\langle \tilde{h}_i(t) \right\rangle &= 0 \\ \left\langle \tilde{h}_{i,\alpha} \tilde{h}_{i,\beta}(t) \right\rangle &= \delta_{\alpha\beta} \end{aligned} \tag{3.6}$$

where α and β denote Cartesian components, k_B is Boltzmann's Constant, and $\tilde{h}_i$ is a Gaussian random variable with mean zero and variance one. Note that in Eq. (3.6), the stochastic term $\tilde{h}_i$ has a coefficient which contains the friction coefficient ζ. This coefficient term is the stochastic force f for a target temperature T and a time step δt. Since the target temperature is specified for each atom, we characterize the Langevin thermostat as local. One downside to

the Langevin thermostat is a lack of feedback between the target temperature and input temperature. While this is reasonable for equilibrium thermostatting, there is no guarantee that the target temperature will be achieved far from equilibrium [82].

Having defined the force by Eq. (3.6), we can include it in an implementation of the velocity Verlet algorithm in the C++ code. We perform the discretisation used in the very popular MD code LAMMPS (Large-scale Atomic/Molecular Massively Parallel Simulator) [83]:

$$\begin{aligned} v_i\left(t+\frac{\delta t}{2}\right) &= v_i(t) - \frac{\delta t}{2}\left(\frac{\nabla_i V(t)}{m} + \zeta v_i(t)\right) + \sqrt{\frac{\delta t k_B T \zeta}{m}}\tilde{h}_i \\ x_i(t+\delta t) &= x_i(t) + v_i\left(t+\frac{\delta t}{2}\right)\delta t \\ v_i\left(t+\delta t\right) &= v_i\left(t+\frac{\delta t}{2}\right) - \frac{\delta t}{2}\left(\frac{\nabla_i V(t+\delta t)}{m} + \zeta v_i\left(t+\frac{\delta t}{2}\right)\right) + \sqrt{\frac{\delta t k_B T \zeta}{m}}\tilde{h}_i \end{aligned} \quad (3.7)$$

where we note that because of the Verlet scheme, the time step in each velocity update is now $\frac{\delta t}{2}$ rather than δt. We generate a different random vector for each particle during each velocity update.

To ensure force matching across the WA and CA regions, we specify the damping factor, ζ, to be a function of position relative to the A/C interface for the Langevin thermostat. To this end, we utilize the equation developed in [46] which linearly ramps the damping in the CA region as the distance from the A/C interface increases. This equation is given as follows:

$$\zeta = \zeta_0\left[1 - \frac{d\left(x\right)}{\omega}\right] \quad (3.8)$$

where ζ_0 equals the maximum damping of 1/2 the Debye frequency of Cu and ω is the length of the CA region. Here, *d* is the minimum distance from the atom at position *x* to the end of the chain (either point x_0 or x_F),

$$d\left(x\right) = abs\left(x_i - x_0\right), abs\left(x_i - x_F\right). \quad (3.9)$$

Hence, for atoms in the CA regions, the damping coefficient varies linearly from zero at the A/C interface to ζ_0 at the ends of the chain. This "stadium" damping allows waves of a variety

of wavelengths to enter the CA region and slowly be absorbed as they propagate to the end of the chain. This reduces spurious wave reflections and artificial waves introduced at the A/C interface.

3.4.2 Nose-Hoover thermostat

The Nose-Hoover thermostat is a deterministic thermostat that introduces a fictitious dynamical friction variable, ζ, which either increases or decreases the particle velocity until the desired temperature is achieved. The Nose-Hoover thermostat is used for many NVT simulations because of its symplectic, volume-conserving, time-reversible Hamiltonian structure [84]. The equations of motion in 1D are as follows:

$$m\frac{d^2x_i}{dt^2} = f_i - \zeta m v_i \tag{3.10}$$

$$\frac{d\zeta\left(t\right)}{dt} = \frac{1}{Q}\left[\sum_{i=1}^{N} m\frac{v_i^2}{2} - \frac{N+1}{2}k_B T\right] \tag{3.11}$$

where Q in Eq. (3.11) determines the relaxation of the dynamics of friction, $\zeta\left(t\right)$, and T is the target temperature. This thermostat preserves the average kinetic energy of the particle ensemble over time and hence is a global thermostat. Unlike the Langevin thermostat, Nose-Hoover cannot control the temperature distribution within the CA region but rather preserves the average temperature [85]. This can be advantageous since the temperature is controlled by a feedback between the calculated and target temperatures, and thus even non-equilibrium simulations will achieve an average temperature.

We make a small modification of the velocity Verlet algorithm to implement the equations of motion of the Nose-Hoover thermostat. The first four steps are as follows:

$$\begin{aligned}
x_i(t+\delta t) &= x_i(t) + v_i(t)\delta t + \left(\frac{f_i(t)}{m} - \zeta(t)v_i(t)\right)\frac{\delta t^2}{2} \\
v_i\left(t+\frac{\delta t}{2}\right) &= v_i(t) + \frac{\delta t}{2}\left(\frac{f_i(t)}{m} - \zeta(t)v_i(t)\right) \\
f_i(t+\delta t) &= f_i(x_i(t+\delta t)) \\
\zeta\left(t+\frac{\delta t}{2}\right) &= \zeta(t) + \frac{\delta t}{2Q}\left[\sum_{i=1}^{N} m\frac{v_i(t)^2}{2} - \frac{N+1}{2}k_BT\right].
\end{aligned} \tag{3.12}$$

We note that $\zeta(t)$ is first updated at time $t+\delta t/2$ to match the two-step character of the velocity Verlet algorithm. The final steps of the Nose-Hoover-Verlet algorithm are

$$\begin{aligned}
\zeta\left(t+\delta t\right) &= \zeta\left(t+\frac{\delta t}{2}\right) + \frac{\delta t}{2Q}\left[\sum_{i=1}^{N} m\frac{v_i\left(t+\frac{\delta t}{2}\right)^2}{2} - \frac{N+1}{2}k_BT\right] \\
v_i(t+\delta t) &= \frac{\left[v_i\left(t+\frac{\delta t}{2}\right) + \frac{\delta t}{2}\frac{f_i(t+\delta t)}{m}\right]}{1+\frac{\delta t}{2}\zeta(t+\delta t)}
\end{aligned} \tag{3.13}$$

where in the last equation, the dissipative force over mass term is computed at time $t+\delta t$.

Chapter 4

Moving Window Formulation

Purely MD simulations of shock wave propagation are limited by small domain sizes and the resulting reflections from the boundaries. To circumvent these issues, we implement a moving window formulation inspired from [56] and [57] into the proposed framework. Such a formulation allows for a detailed investigation of the shock wave jump conditions and EOS from an atomistic scale with minimal influence from spurious wave reflections. The moving window atomistic method is outlined in Fig. 4.1.

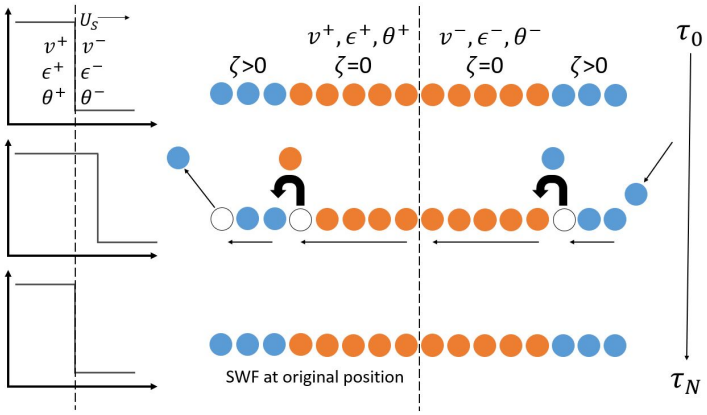

Figure 4.1: Schematic of the moving window mechanism for a shock wave propagating through a 1D chain of atoms.

The proposed work feeds a constant flux of material with mean unshocked particle velocity, strain, and temperature of $(v^-, \epsilon^-, \theta^-)$ into the simulation window by inserting atoms at the right boundary (x_F) with a frequency of $\tau^{-1} = U_S/a_0$, where a_0 is the equilibrium spacing of Cu. In other words, after the shock wave has traveled a distance of one lattice constant, the program adds a single Cu atom to the right CA region while simultaneously removing a

single Cu atom from the left CA region. At the same time, the window atom at $x_{WA,0}$ is added to the left CA region while the boundary atom at $x_{WA,F}$ is added to the rightmost position within the WA region. In effect, every atom in the chain shifts to the left by one equilibrium lattice spacing when $\tau = N(a_0/U_S)$, where N increases by one each time the shock travels a distance of a_0. Fig. 4.1 shows a schematic of this process of adding, removing, and shifting atoms. Local atomic energy fluctuations induced near the right boundary of the chain from the atom addition are damped by either the Langevin or Nose-Hoover thermostat to establish the prescribed temperature θ^- as described previously. After a stationary shock is established, the material flux through the system is automatically conserved.

An $x - t$ diagram of the moving window process is presented in Fig. 4.2. An idealized shock wave with speed U_S originates at $(x, t) = (0, 0)$ and travels into the initially undisturbed material. When the simulation begins, the SWF is located at the center of the WA region. We start the simulation with atoms in the WA regions ahead of and behind the shock initialized with (v^-, ϵ^-) and (v^+, ϵ^+) respectively, and in the CA regions ahead of and behind the shock with $(v^-, \epsilon^-, \theta^-)$ and $(v^+, \epsilon^+, \theta^+)$ respectively. As the simulation evolves in time, the shock wave propagates forward through the material. During this time, the moving window process occurs with a frequency $\tau^{-1} = U_S/a_0$, and the atomistic domain "follows" the propagating shock. This ensures that the SWF remains at the center of the WA region. Ordinarily, the shock would propagate forward towards the A/C interface and eventually travel out of the whole domain, thus limiting the simulation time. In contrast, the moving window formulation allows us to perform extremely long-time steady state shock propagation simulations.

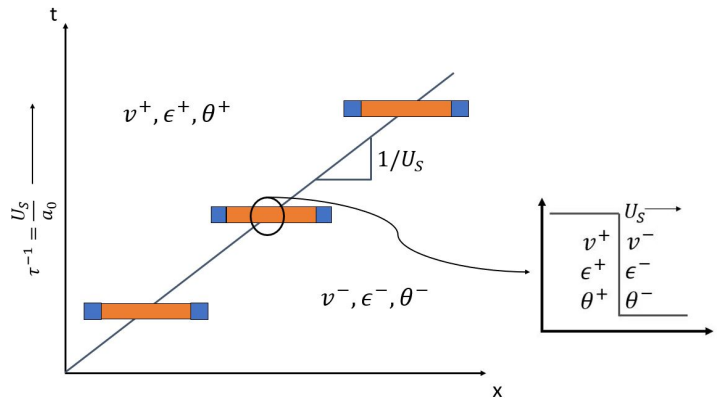

Figure 4.2: X-t diagram representation of the moving window formulation.

Semi-infinite boundary conditions are implemented as stated in Ch. 3.1, and the process by which the atomistic domain "follows" a propagating shock limits the number of interactions from transient waves. Many of these transient waves will be absorbed into either of the CA regions and thus damped out of the system. Those that are reflected off the left A/C interface will have to travel at a speed greater than the insertion frequency of the moving window to eventually interact with the shock wave. Hence, while this framework does not completely eliminate effects from spurious wave reflections, the implementation of a moving window within the atomistic framework drastically limits their influence on the shock. The moving window atomistic method differs from standard MD simulations by treating the complex processes behind the SWF for an indefinite period of time without the total number of atoms continually increasing as the simulation evolves.

Chapter 5

Verifications

5.1 NVT Ensemble

We perform time integration on Langevin or Nose-Hoover non-Hamiltonian equations of motion designed to generate positions and velocities sampled from a canonical (NVT) ensemble. A canonical ensemble represents the possible states of a system in thermal equilibrium with a heat bath at a given temperature [86]. The system may differ in total energy as such energy may be exchanged with the heat bath. Hence, our MD simulations should maintain a constant temperature using either the Langevin or Nose-Hoover thermostat which are designed to maintain a system at thermal equilibrium.

Temperature is a macroscopic quantity, and thus it is less well-defined microscopically due to the low number of particles. However, if we calculate the kinetic energy, we can compute the temperature by

$$KE = \frac{1}{2}mv_i^2 = \frac{dim}{2}Nk_BT. \tag{5.1}$$

Here, $dim = 1$, N is the total number of atoms, and KE is the total kinetic energy of the group of atoms $\sum \frac{1}{2}mv_i^2$. We can use Eq. (5.1) to calculate the average temperature of the system as a function of time.

We perform constant temperature simulations for systems of 10,000 Cu atoms using both the Langevin and Nose-Hoover thermostats. We test the performance of each of these thermostats using all three potential functions (LJ, modified Morse, and EAM) at temperatures ranging from 250 K - 1,250 K. Since the melting temperature of Cu is 1,358 K, we do not perform simulations with higher input temperatures. The total run-time for each simulation is

3,000 ps (3 ns) with an equilibration time of 5 ps. In this case, standard periodic boundary conditions are enforced such that the leftmost atom interacts with the rightmost atom in the chain and vice versa. Therefore, we do not enforce the A/C domain described in Fig. 3.1. The results from these MD simulations can be seen in Fig. 5.1.

For all three potential functions, the average temperatures oscillate around their corresponding initial input values for the entire run-time of 3,000 ps. However, we notice that for each thermostat, the variance in the average temperature increases with increasing input temperature. This effect occurs regardless of which potential function is used. Such a phenomenon makes physical sense because the frequency of oscillation of the particles in a solid increases as the temperature in the solid is raised. Additionally, we observe that at higher temperatures, the Nose-Hoover thermostat equilibrates the system to the initial input temperature slightly faster than the Langevin thermostat. This effect is seen for all three potential functions, and it is most prominent at an input temperature of 1,250 K. This is understandable as the Langevin thermostat is a local thermostat, and hence there is a lack of feedback between the target temperature and input temperature. However, the Nose-Hoover thermostat is global and thus preserves the average temperature over time by providing a feedback between the calculated and target temperature. From these results, it is apparent that we maintain a canonical (NVT) ensemble for a wide range of input temperatures using both the Langevin and Nose-Hoover thermostats.

5.2 Mechanical properties

Verification of the Lennard-Jones and modified Morse potentials is carried out by computing the tangent modulus of the system over a range of temperatures, while verification of the EAM potential is achieved by computing the cohesive energy and bulk modulus of the system at 0 K. In each case, we compare the simulated mechanical properties to their corresponding literature values for Cu.

5.2.1 LJ and Morse potentials

To compute the isothermal elastic modulus in 1D (tangent modulus), we utilize the microscopic elasticity tensor derived in [30]. We note, however, that depending on the loading conditions,

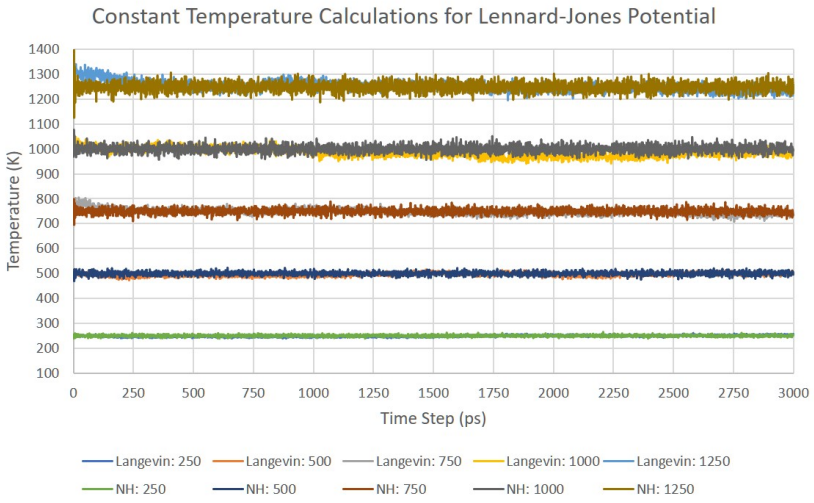

(a)

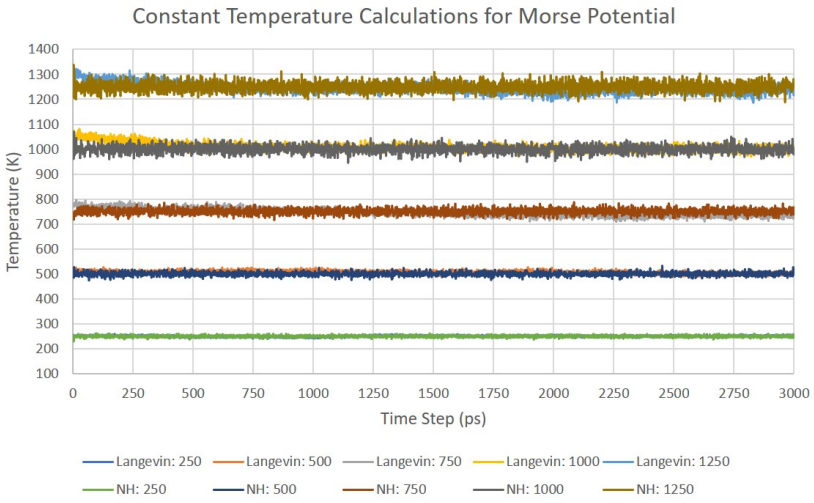

(b)

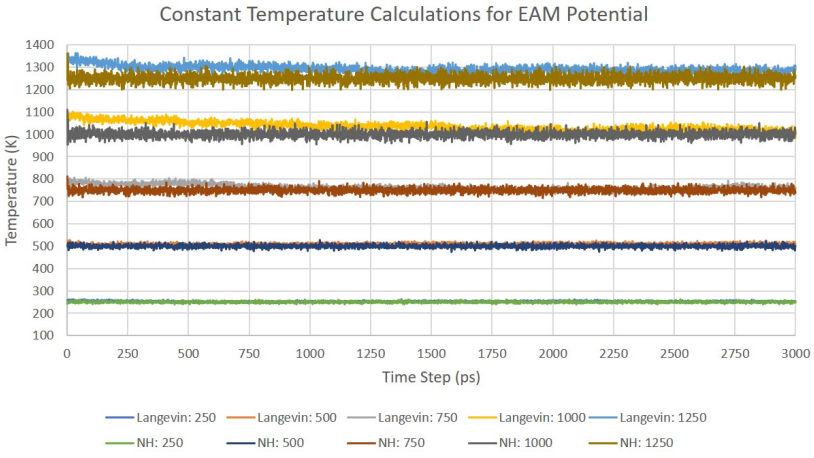

(c)

Figure 5.1: Constant temperature NVT results for the Langevin and Nose-Hoover thermostats using (a) Lennard Jones, (b) Morse and (c) EAM potentials.

there are two separate elasticity tensors. If the material is loaded rapidly, there is not enough time for the material to exchange heat internally or with the surroundings. In this case, the *adiabatic* elasticity tensor derived from the internal energy is utilized. However, when the material is loaded slowly, it has enough time to reach thermal equilibrium with the surroundings. In this case, the *isothermal* elasticity tensor derived from the Helmholtz free energy is utilized. As shown in [87], the two tensors are equal at $T = 0$ K, but the discrepancy increases with temperature. In our case, the microscopic elasticity tensor is derived from the Helmholtz free energy and is thus isothermal.

The conventional expression for the microscopic elasticity tensor at a temperature *T* is given as follows [30]:

$$c_{ijkl} = \frac{1}{V}\left[2Nk_BT\left(\delta_{il}\delta_{jk} + \delta_{jl}\delta_{ik}\right) + \left\langle c^0_{ijkl}\right\rangle - \frac{V^2}{k_BT}Cov\left(\sigma^{inst}_{ij}, \sigma^{inst}_{kl}\right)\right] \tag{5.2}$$

where $\langle\cdot\rangle$ refers to a *phase* average, k_B is Boltzmann's Constant, *V* is the volume, and the covariance operator is defined by

$$Cov\left(A, B\right) \equiv \langle AB\rangle - \langle A\rangle\langle B\rangle . \tag{5.3}$$

Additionally, c^0_{ijkl} is defined as

$$c^0_{ijkl} = \frac{1}{V}\left[\frac{1}{4}\sum_{\alpha\neq\beta}\sum_{\gamma\neq\delta}\kappa^{\alpha\beta\gamma\delta}\frac{r^{\alpha\beta}_i r^{\alpha\beta}_j r^{\gamma\delta}_k r^{\gamma\delta}_l}{r^{\alpha\beta}r^{\gamma\delta}} - \frac{1}{2}\sum_{\alpha\neq\beta}\phi^{\alpha\beta}\frac{r^{\alpha\beta}_i r^{\alpha\beta}_j r^{\alpha\beta}_k r^{\alpha\beta}_l}{\left(r^{\alpha\beta}\right)^3}\right] \tag{5.4}$$

where $\phi^{\alpha\beta}$ is the interatomic force depending only on the distance $r^{\alpha\beta}$ between the atoms, and $\kappa^{\alpha\beta\gamma\delta}$ is the *bond stiffness* defined by

$$\kappa^{\alpha\beta\gamma\delta} \equiv \frac{\partial\phi^{\alpha\beta}}{\partial r^{\gamma\delta}} = \frac{\partial^2 V^{int}}{\partial r^{\alpha\beta}\partial r^{\gamma\delta}}. \tag{5.5}$$

This bond stiffness is interpreted for a simple pairwise potential, where the force on atom α due to atom β depends only on the distance $r^{\alpha\beta}$. Equation (5.2) can be further simplified by

splitting the instantaneous stress terms into kinetic and potential parts as seen below:

$$\sigma_{ij}^{K,inst} = -\frac{1}{V}\sum_{\alpha}\frac{p_i^{\alpha}p_j^{\alpha}}{m^{\alpha}}$$
$$\sigma_{ij}^{V,inst} = \frac{1}{2V}\sum_{\alpha\neq\beta}\phi^{\alpha\beta}\frac{r_i^{\alpha\beta}r_j^{\alpha\beta}}{r^{\alpha\beta}}. \tag{5.6}$$

Substituting $\sigma^{inst} = \sigma^{K,inst} + \sigma^{V,inst}$ into the third term of Eq. (5.2) and noting that the cross-terms cancel,

$$\left\langle \sigma_{ij}^{K,inst}\sigma_{ij}^{V,inst}\right\rangle = \left\langle \sigma_{ij}^{K,inst}\right\rangle\left\langle \sigma_{ij}^{V,inst}\right\rangle \tag{5.7}$$

we get the following:

$$Cov\left(\sigma_{ij}^{inst},\sigma_{kl}^{inst}\right) = Cov\left(\sigma_{ij}^{K,inst},\sigma_{kl}^{K,inst}\right) + Cov\left(\sigma_{ij}^{V,inst},\sigma_{kl}^{V,inst}\right). \tag{5.8}$$

Then, as shown in [30], the kinetic terms can be reduced as follows:

$$Cov\left(\sigma_{ij}^{K,inst},\sigma_{kl}^{K,inst}\right) = \left(\delta_{ik}\delta_{jl}+\delta_{il}\delta_{jk}\right)N\left(k_BT\right)^2. \tag{5.9}$$

Substituting Eqs. (5.8) and (5.9) into Eq. (5.2), we get the simpler form of the elasticity tensor:

$$c_{ijkl} = \frac{1}{V}\left[\left\langle c_{ijkl}^0\right\rangle - \frac{V^2}{k_BT}Cov\left(\sigma_{ij}^{V,inst},\sigma_{kl}^{V,inst}\right) + Nk_BT\left(\delta_{ik}\delta_{jl}+\delta_{il}\delta_{jk}\right)\right]. \tag{5.10}$$

Here, the first term is the elasticity at 0 K, the second term is the instantaneous potential energy, and the third term is the instantaneous kinetic energy. It is noted that the third term goes to zero as $T \rightarrow 0$ K. Additionally, [88] showed that the fluctuation term disappears as the stress and potential terms expand. In this case, $c = c^0$, where c^0 is given by Eq. (5.4). We note that the elastic constants associated with shear vanish in the thermodynamic limit, as shown in [89]. However, Eq. (5.10) still allows us to calculate the elastic constants of solids by replacing the phase averages with time averages.

The method just described to calculate the spatial elastic modulus is known as the stress fluctuation method [90, 91, 92]. We use this stress fluctuation method to calculate the microscopic elastic (tangent) modulus of a one-dimensional chain of Cu atoms with constant length *L* and constant temperature *T*. For the 1D case, Eq. (5.10) reduces to the following [73]:

$$c = \frac{1}{L}\left[2Nk_BT + L\left\langle c^0\right\rangle - \frac{L^2}{k_BT}Cov\left(\sigma^{V,inst}, \sigma^{V,inst}\right)\right] \tag{5.11}$$

where *L* is the chain length, and *"Cov"* is the covariance operator given by Eq. (5.3). Then, the c^0 Born term in 1D is

$$c^0 = \frac{1}{L}\sum_{i=1}^{N}\sum_{j=i+1}^{N}\left[\phi''(x_{ij})(x_{ij})^2 - \phi'(x_{ij})x_{ij}\right] \tag{5.12}$$

where $x_{ij} = x_j - x_i$. Finally, the potential part of the instantaneous stress in 1D is given as follows:

$$\sigma^{V,inst} = \frac{1}{L}\sum_{i=1}^{N}\sum_{j=i+1}^{N}\phi'(x_{ij})x_{ij}. \tag{5.13}$$

We compare the tangent modulus obtained from MD to the tangent modulus obtained from the Quasi-Harmonic (QH) approximation. The QH approximation for the temperature-dependent stress-free spatial tangent modulus of a 1D chain of atoms is [30, 73]:

$$c = a\left[\phi''(a) + \frac{k_BT}{2}\frac{\phi^{(4)}(a)\phi''(a) - (\phi'''(a))^2}{(\phi''(a))^2}\right] \tag{5.14}$$

where $a = a(T)$ is the stress-free equilibrium lattice constant at temperature *T*. In this case, the temperature dependence of the equilibrium lattice constant is obtained through the following equation [30]:

$$\phi'(a) + \frac{k_BT}{2}\frac{\phi'''(a)}{\phi''(a)} = 0. \tag{5.15}$$

This requires calculation of third and fourth derivatives of the potential function ϕ, making calculations for EAM cumbersome. We use Eq. (5.14) to obtain the analytic tangent modulus values for the Lennard-Jones and modified Morse potentials.

We utilize Eq. (5.11) to calculate the microscopic tangent modulus of a one-dimensional chain of 10,000 Cu atoms using the Lennard-Jones and modified Morse potential functions. We test the performance of each of these potentials for both of the thermostats at various temperatures. For each of the input temperatures, we calculate the corresponding equilibrium lattice spacing using Eq. (5.15). Using these temperature-dependent lattice spacings, we can obtain the tangent modulus from MD simulations with Eq. (5.11) and compare this to the tangent modulus obtained analytically with Eq. (5.14). Plots showing the MD and analytic tangent modulus results can be seen in Fig. 5.2.

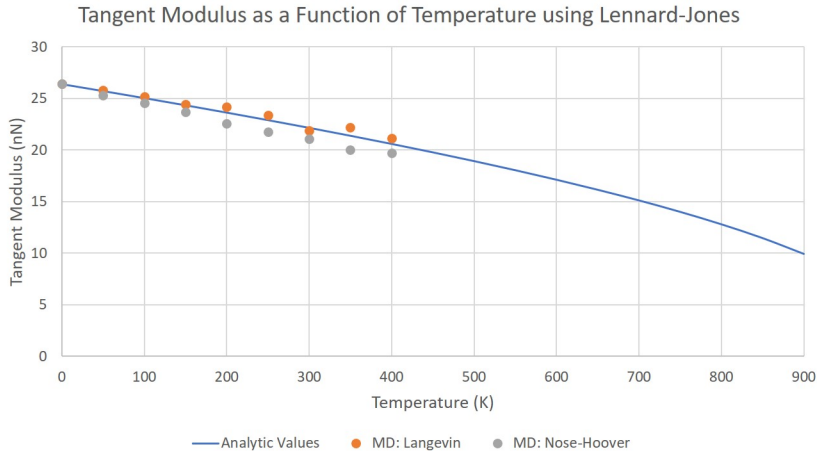

(a)

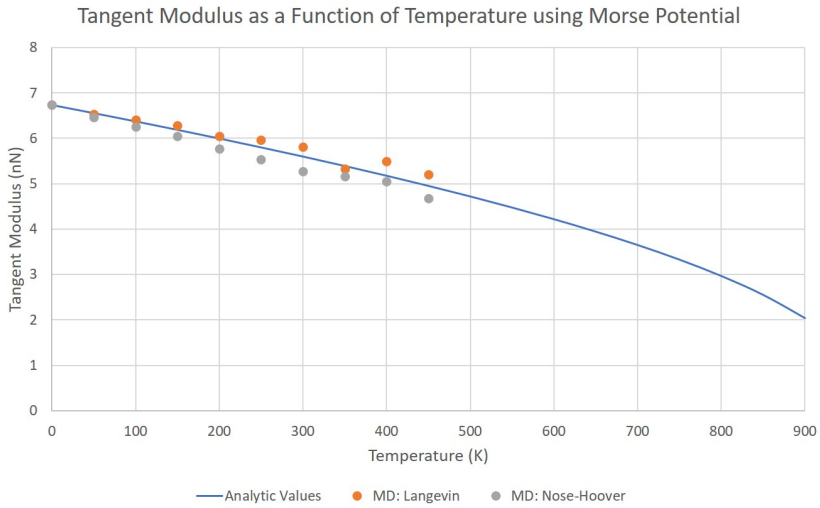

(b)

Figure 5.2: Tangent modulus results for the Langevin and Nose-Hoover thermostats using the (a) Lennard-Jones and (b) Morse potentials.

Here, we show the analytic tangent modulus values (blue line) for temperatures ranging from 0 - 900 K, but we limit the MD calculations for LJ and Morse to 400 K and 450 K respectively. As shown in [73], the MD-derived tangent modulus of the system becomes non-physical for input temperatures above $\approx$ 450 K. The total run-time for each MD simulation is 3,000 ps (3 ns) with an equilibration time of 10 ps. As in Ch. 5.1, each atom is treated as a continuum atom, and normal periodic boundary conditions are enforced such that the leftmost atom interacts with the rightmost atom and vice versa. The MD results for both the Lennard-Jones and Morse potentials are plotted in increments of 50 K and are seen to be in close agreement with the values obtained from the QH approximation. This validates the implementation of the Lennard-Jones and modified Morse potentials in the code.

5.2.2 EAM potential

To verify the EAM potential, we calculate the cohesive energy E_0 as well as the bulk modulus B of the system at 0 K. Again, the cutoff radius for the EAM potential is *5.507* $\mathring{A}$, and we consider a periodic chain of 500 atoms where each atom is treated as a window atom. The experimental value of the equilibrium lattice spacing of Cu is *3.615* $\mathring{A}$, so we vary the lattice constant from *3.605* $\mathring{A}$ to *3.625* $\mathring{A}$ in steps of *0.001* $\mathring{A}$. The potential energy per atom as a function of the cubic lattice spacing is plotted in Fig. 5.3, and the data can be fitted to a parabola. The minimum of this parabola corresponds to the cube of the equilibrium lattice

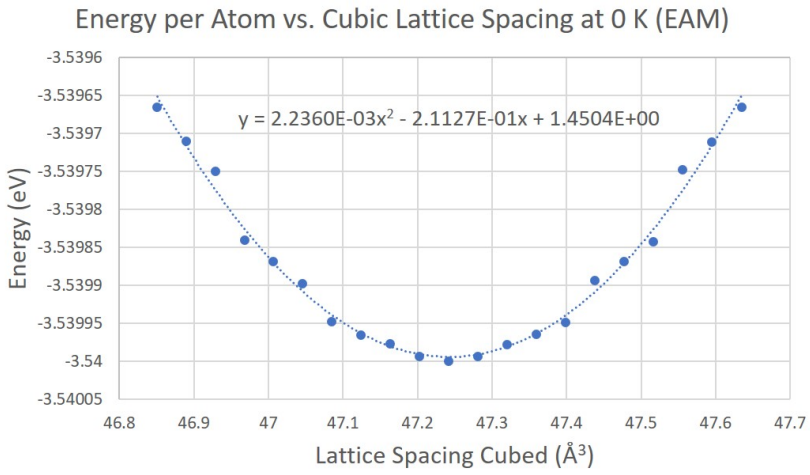

Figure 5.3: Potential energy per atom vs. cubic lattice spacing in steps of *0.001* $\mathring{A}$. Circles are data computed from the EAM potential, and the line is a parabola fitted to the data.

spacing, $a_0 = 3.615\ \mathring{A}$. This matches the experimental data perfectly because a_0 is one of the fitted parameters of the EAM potential. The energy per atom at a_0 is the cohesive energy, $E_{coh} = -3.540\ eV$, which is another fitted parameter [77]. Hence, our implementation of the EAM potential gives an accurate representation of the cohesive energy of Cu.

As discussed in [93], the curvature of the parabola at a_0 can be used to calculate the bulk modulus using

$$B(V) = V\left(\frac{\partial^2 E}{\partial V^2}\right)_{T,S} = 4(a_0)^3(2a) \tag{5.16}$$

where a is the parabola coefficient, and we multiply by four to account for every atom in the given lattice volume. Applying this equation to the data in Fig. 5.3, we obtained a bulk modulus value of $B = 135.4$ GPa, which is not very accurate when compared to the literature value of *140* GPa [77]. To obtain a more accurate bulk modulus, we compute the $E(V)$ curve again in the range of $|a - a_0| < 10^{-4}\ \mathring{A}$. Specifically, we perform the calculations in steps of $0.0008\ \mathring{A}$. This plot can be seen in Fig. 5.4. The curvature of this new parabola at a_0 gives a bulk modulus value of $B = 140.6$ GPa, which is the fitted bulk modulus of this potential model.

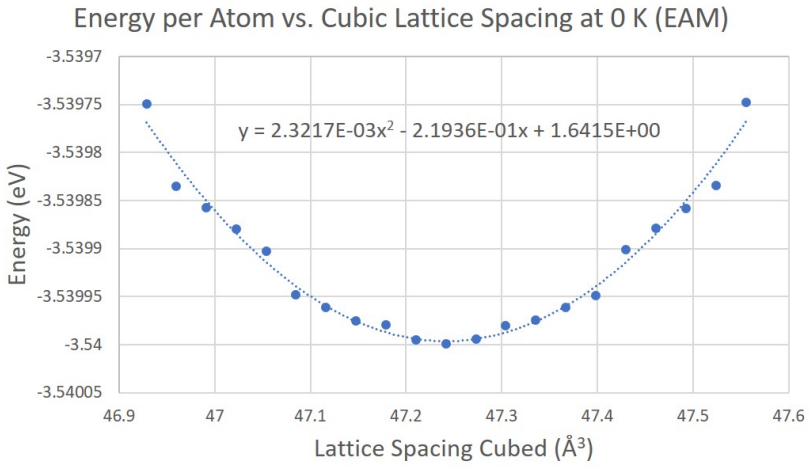

Figure 5.4: Potential energy per atom vs. cubic lattice spacing in steps of *0.0008* $\mathring{A}$. Circles are data computed from the EAM potential, and the line is a parabola fitted to the data.

5.3 Steady State

The moving window framework is verified by confirming that entire A/C domain reaches steady state after a long period of time. Typically with A/C frameworks, a bi-material interface is

formed which can lead to numerical errors as shown in [41]. Hence, there exists a need to smoothly exchange information (e.g. defects, heat, and waves) from specifically the atomistic to the continuum domain. Since there are more DOFs in atomistics [94], the reverse exchange (continuum to atomistic domain) is relatively more fluent. For these reasons, we must ensure that the WA region smoothly transfers information to the CA regions. A lack of smooth information exchange would introduce non-physical effects into the WA region such as a rise in particle velocity and associated temperature and/or traveling waves.

To ensure that the WA/CA interfaces are not introducing spurious waves into the WA region, we prescribe the same continuum states to both CA regions. In other words, the problem has now moved either to the left of the shock or the right of the shock in Figure 4.2. As the simulation evolves, there should be no traveling waves after a reasonable interval of time. Such artifacts would mean that waves are not being smoothly absorbed into the CA regions and instead impinging off the WA/CA interface, and/or the periodic boundary conditions are improperly implemented. Additionally, the average particle velocity of the system should remain equal to the initial input value with little to no increase in the average amplitude. A change in the average particle velocity would indicate that the system is not reaching equilibrium, while a large increase in amplitude would mean that energy is being artificially added to the system.

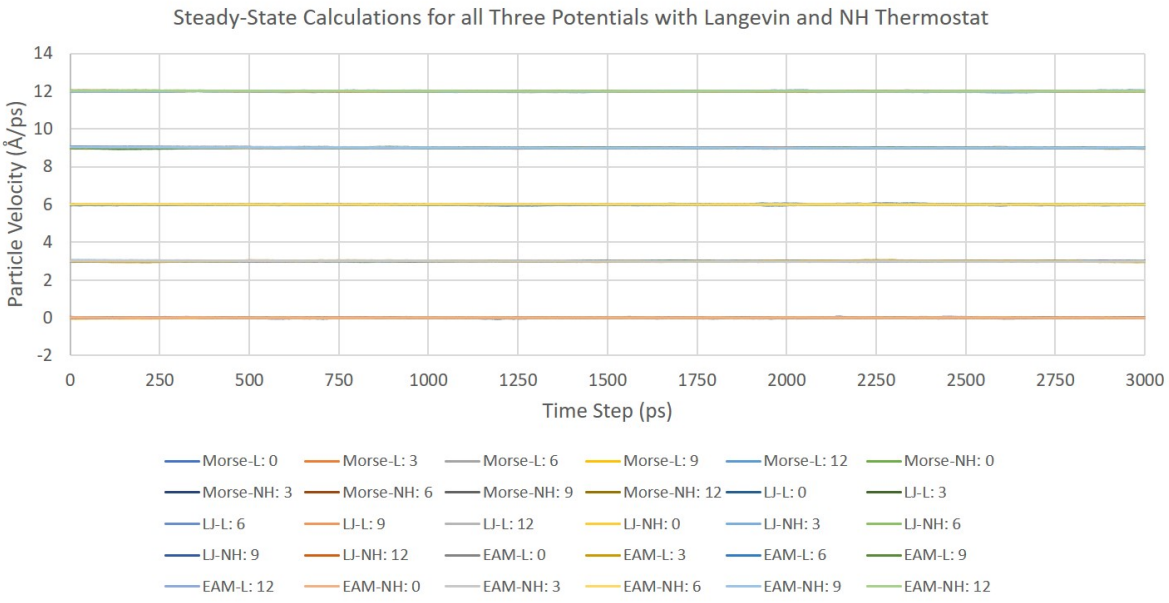

Figure 5.5: Average particle velocity of different systems vs. time for a range of input velocities.

We perform steady state simulations for one-dimensional systems of 10,000 Cu atoms using all three potential functions and both thermostats. We utilize the moving window atomistic framework described in Chs. 3 and 4 with 100 atoms in each CA region and 9,800 atoms in the WA region. Placing 100 atoms in each CA region ensures that waves impinging on the WA/CA interfaces can fully dissipate into the CA regions. This improves the absorption of energetic pulses into the CA regions and thus helps reduce the number of wave reflections into the WA region. We test the implementation of these interfaces for various mean particle velocities: $0, 3, 6, 9,$ and 12 $\mathring{A}/ps$. The results from these simulations can be seen in Fig. 5.5, where we plot the average particle velocity of the 1D system vs. time. As before, the total run-time for each simulation is 3,000 ps (3 ns), and we enforce periodic boundary conditions as explained in Ch. 3.1. It is apparent that regardless of the potential function or thermostat used, the system maintains the initial mean particle velocity for the duration of the simulation. From these results, we conclude that the WA region achieves steady state for long-time simulations.

Finally, we confirm that the average amplitude of the particle velocities remains relatively constant and no large traveling waves appear throughout the duration of the simulation. Figs. 5.6, 5.7, and 5.8 show six different particle velocity vs. particle number plots for all three potentials using both thermostats. In each of these graphs, we plot the velocity of each particle at 0 ps and overlay that with the velocity of each particle at $3,000$ ps for each input velocity ($0, 3, 6, 9,$ and 12 $\mathring{A}/ps$). We overlay these sets of data from the beginning and end of the simulation to observe how the average amplitude changes over time. We observe that in each case, the amplitude of the particle velocities does not increase as the simulation evolves. In fact, the two sets of data overlap each other almost identically indicating that no artificial energy is being introduced into the WA region. (We also note that no large traveling waves were observed in the WA region over the entire run-time). These results confirm that any spurious waves encountering the WA/CA interfaces are traveling smoothly into the CA regions and eventually dissipating. Additionally, the data establish that the periodic boundary conditions used in the CA regions are implemented correctly.

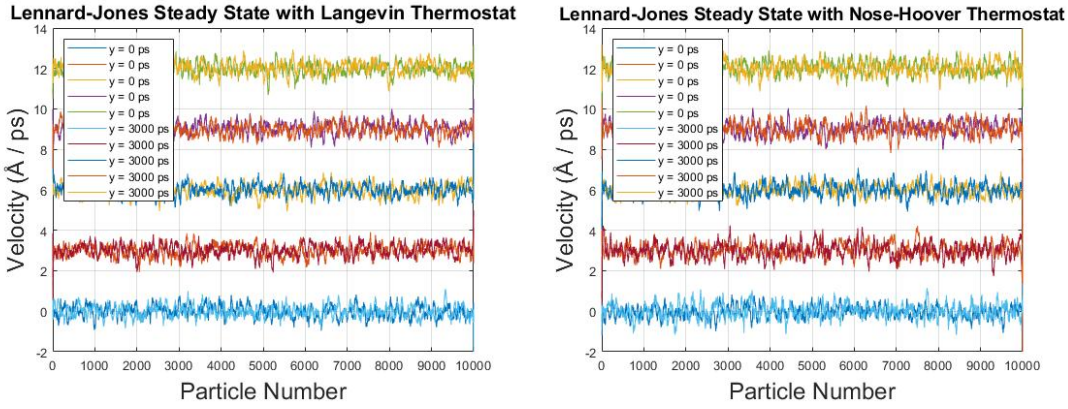

(a) (b)

Figure 5.6: Steady state plots for Lennard-Jones potential with (a) Langevin and (b) Nose-Hoover thermostat.

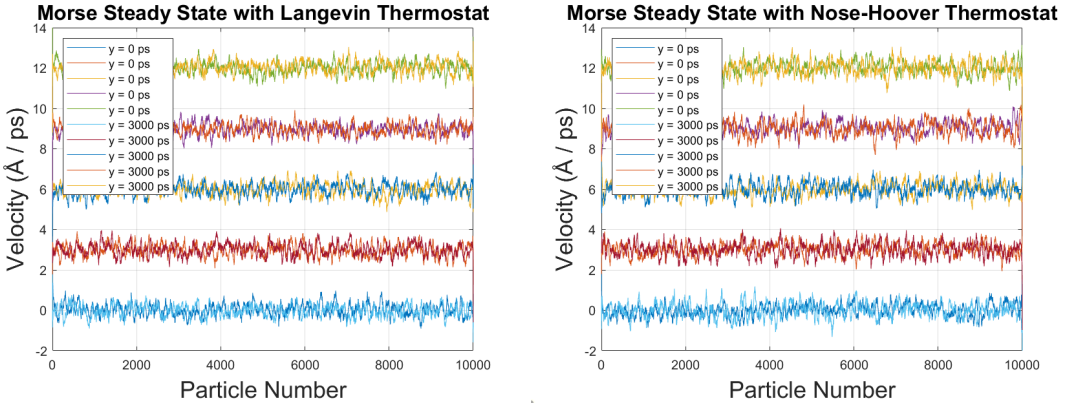

(a) (b)

Figure 5.7: Steady state plots for modified Morse potential with (a) Langevin and (b) Nose-Hoover thermostat.

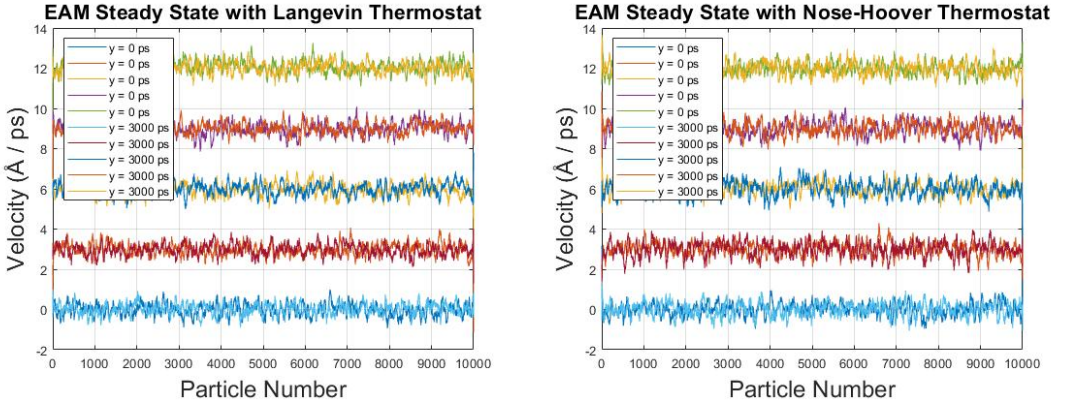

(a) (b)

Figure 5.8: Steady state plots for EAM potential with (a) Langevin and (b) Nose-Hoover thermostat.

Chapter 6

Results

6.1 Moving window simulations with original EOS

Having verified different aspects of the framework, we conduct long-time, large-domain shock simulations for various input shock wave velocities in the [110] close packed direction of a one-dimensional chain of Cu atoms. As before, we use all three potentials and both thermostats. In each simulation, the domain contains a total of 10,000 atoms with 100 atoms in each CA region. Hence, we have a central WA region containing 9,800 atoms and two CA regions each containing 100 atoms. As stated in [46], the width of the CA region should be at least the range of the forces, typically around $10\ \mathring{A}$. We choose a much larger width of 100 atoms ($\approx 256\ \mathring{A}$) to ensure a sufficient distance for any wave traveling from the WA region to the CA regions to be fully absorbed. Additionally, we perform each of these simulations for 3,000 ps (3 ns) in order to track the motion and evolution of the fully-developed wave. As stated in the supplemental material of [57], the total time for shock wave formation and propagation in standard piston simulations is usually limited to $\sim 100\ ps$ or less because the shock wave will leave the domain. Hence, the number of atoms that have to be included grows as the shock moves away from the piston face. However, using the moving window atomistic framework, we can obtain simulation times of $\geq 100\ ps$ which allows us to track the shock wave indefinitely.

We perform a given simulation by choosing the shock wave velocity U_S and initializing the unshocked state of $v^- = 0\ \mathring{A}/ps$, $\epsilon^- = 0$, and $\theta^- = 298\ K$. Then we use the jump equations, thermodynamic relationship, and linear shock EOS presented in Ch. 2 to compute the state $(v^+, \epsilon^+, \theta^+)$ of the shocked material. In Fig. 6.1, we present simulations for an input shock

velocity of $U_S = 50\ \mathring{A}/ps$ using the EAM potential and incorporating the Langevin thermostat (the other potentials/thermostats produce similar results). In this case, we overlay the initial shock wave with its later positions in 100 ps increments, so we see the evolution in time of the shock over a period of 1,000 ps. We employ the moving window formulation as explained in Ch. 4 with an atomic replacement frequency of $\tau^{-1} = U_S/a_0$.

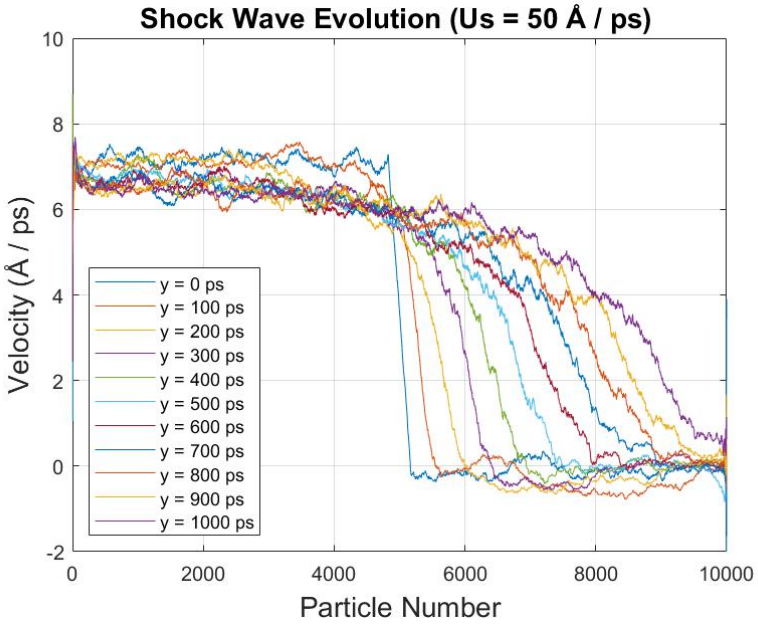

Figure 6.1: Propagation of a shock wave front using the EAM potential with the Langevin thermostat for an input shock velocity of $50\ \mathring{A}/ps$. This simulation was produced using the linear shock relation parameters from literature [1].

The moving window framework should maintain the SWF at the center of the WA region throughout the entire simulation. However, in Fig. 6.1, we observe two discrepancies in the simulated shock wave. First, the SWF continues traveling forward through the chain as the simulation evolves in time despite the moving window implementation. Additionally, the particle velocities in the shocked material (v^+) oscillate around a mean value which is lower than their initial mean value. Hence, we observe that the shock parameters U_S and v^+ obtained from MD are different than their corresponding analytical input values. If we recall the linear relation between shock velocity and particle velocity,

$$U_s = C_0 + S[\![v]\!] \tag{6.1}$$

we deduce that such discrepancies indicate that the empirical parameters for this equation (C_0 and S) are not optimized for our one-dimensional framework. This makes intuitive sense because these empirical parameters are derived through experimental methods assuming a three-dimensional lattice. It should be emphasized that this does not imply that the EOS parameters are incorrect in general. It merely means that the the EOS parameters are not applicable to our one-dimensional framework. In Ch. 6.2, we will obtain the necessary 1D EOS parameters to obtain a stable and steady shock.

We also present a graph of the SWF position vs. time using the EAM potential and Langevin thermostat for the following input shock velocities: $47, 50, 54, 58$ and 60 $\mathring{A}/ps$. From Fig. 6.2, it can be observed that in each case, the shock wave travels to the right, and the speed of this forward motion increases with increasing input shock velocity, U_S. Such a phenomenon implies that the moving window replacement frequency is essentially "under-predicting" the shock wave frequency, and thus the WA region is "falling behind" the forward moving shock. This lack of agreement between the shock wave and moving window becomes more pronounced as the input shock velocity increases. These results again show that the empirical linear EOS parameters are ill-suited for our 1D framework.

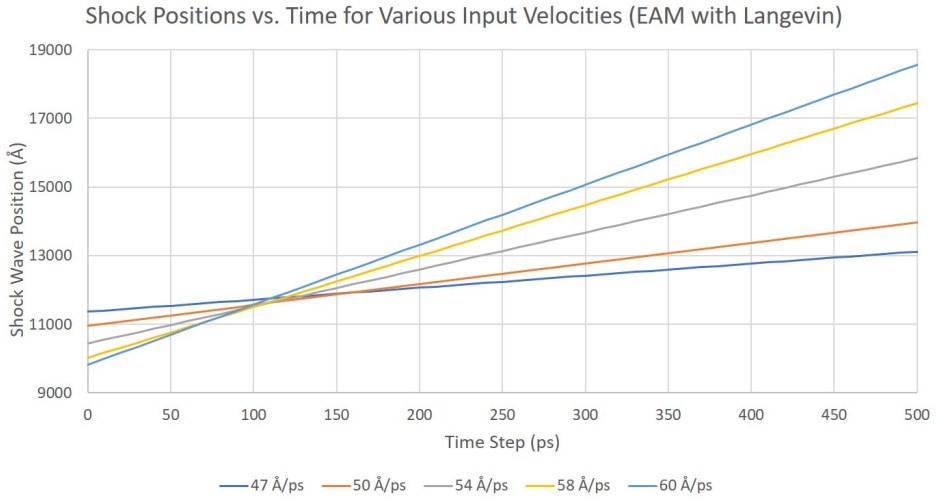

Figure 6.2: Position vs. time of the SWF for various input shock velocities using the EAM potential and Langevin thermostat. These were produced using the shock EOS parameters from literature [1].

A final plot showing the discrepancy between the input and MD shock velocity can be seen in Fig. 6.3. Here, we plot the average momentum of the entire domain vs. time for the

five different input shock velocities mentioned earlier. We display the average momentum of the five trials with solid lines up until the point where the shock wave impinges upon the right WA/CA interface. After this point, the data becomes invalid. We then extrapolate the average momentum up to 3,000 ps (assuming an infinite domain) using a linear fit which is represented in the plot by the dotted lines. From this linear fit, we obtain a linear relation between the average momentum and time for each shock wave trial. We observe that the slopes of the linear equations are non-zero and increase with increasing shock input velocity. Ideally, these slopes would be zero because the shock front would remain at the center of the WA region, and thus the average particle velocity of the domain would remain constant. Since this is not the case, we conclude that the shocks are propagating forward as the simulation evolves in time. In the next section, we produce a 1D linear relation between the SWF velocity and particle velocity to counteract these issues.

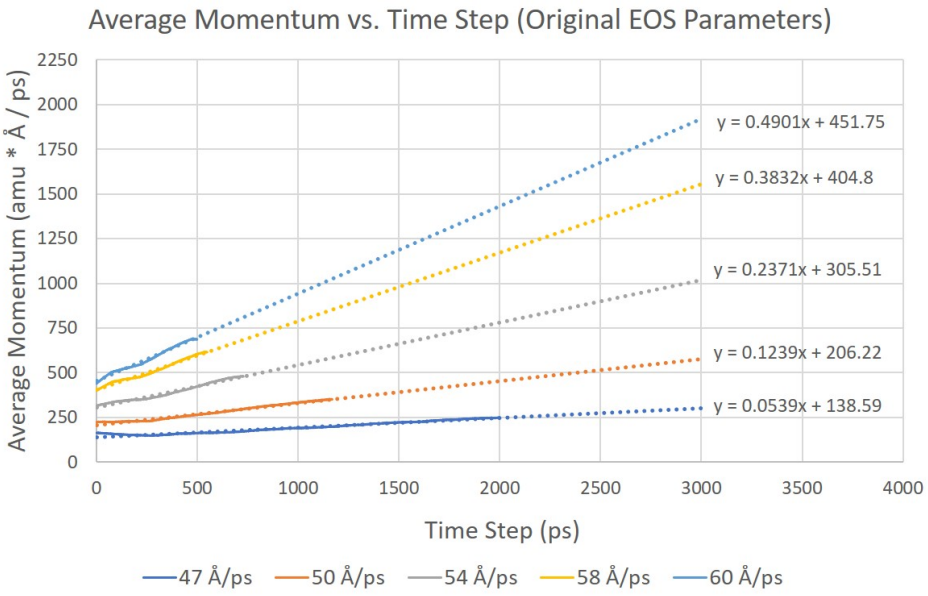

Figure 6.3: Average momentum vs. time of the entire domain for various input shock velocities using the EAM potential and Langevin thermostat. These simulations were produced using the EOS parameters from literature [1].

6.2 New EOS calculations

To derive new empirical parameters for the linear shock EOS, we analyze moving window shock simulations using all three potentials and both thermostats for the following input shock

velocities: $47, 50, 54, 58$, and 60 $\mathring{A}/ps$. Specifically, we track the position of the SWF as well as the mean particle velocity behind the SWF until the shock impinges upon the right WA/CA interface (analysis is invalid after this point). In Fig. 6.4, we observe a snapshot at 35 ps of a propagating shock with an input velocity of 60 $\mathring{A}/ps$. We observe four main components to this shock plot: the mean particle velocity behind the SWF (v^+) derived from Eq. (2.13), the actual mean particle velocity behind the SWF, the position of the SWF, and the mean particle velocity input by the user in the un-shocked material (v^-). It can be observed that the actual v^+ is slightly higher than the analytical v^+ which results in the actual ϵ^+ in the shocked material being higher than the analytical ϵ^+. This phenomenon causes the moving window replacement frequency to under-predict the shock wave frequency, and this results in a forward propagating shock wave. Therefore, because of the incorrect linear EOS parameters, the actual shock parameters (v^+, ϵ^+, and U_S) are different from their corresponding analytical values.

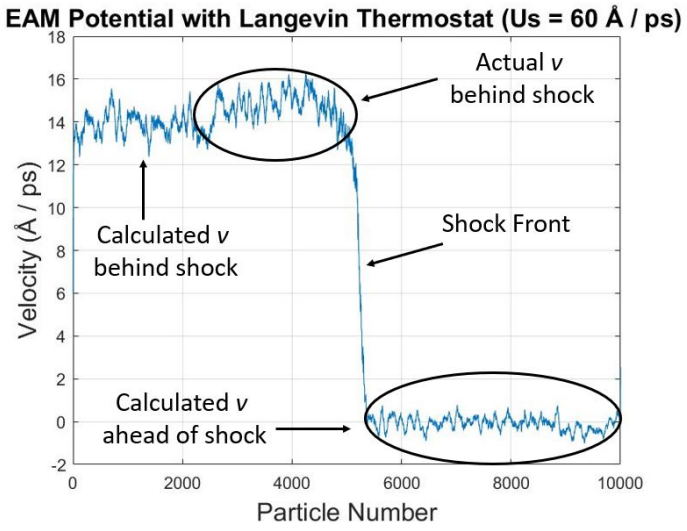

Figure 6.4: Snapshot at 35 ps of a propagating shock with an input shock velocity of 60 $\mathring{A}/ps$.

We plot the average shock velocity vs. particle velocity of the five shock wave trials for each of the potentials and thermostats. These results can be seen in Fig. 6.5. The slope of each linear fit is the new S value while the y-intercept is the new C_0 value. The Langevin and Nose-Hoover thermostats produce nearly identical results, so we will only analyze the results obtained using the Langevin thermostat. We observe that the EAM and modified Morse potentials produce the most accurate values when compared to the original EOS parameters.

EAM produces C_0 and S values of approximately $35.77\ \mathring{A}/ps$ and 2.84 respectively while Morse produces values of $43.56\ \mathring{A}/ps$ and 2.57 respectively. Hence, EAM slightly under-predicts while Morse slightly over-predicts the original C_0 value of $39.4\ \mathring{A}/ps$. The S value for materials is typically between 1 and 2, so we attribute the difference in our calculations to 1D effects. In contrast to EAM and Morse, the LJ potential produces very inaccurate results, giving C_0 and S values of $55.68\ \mathring{A}/ps$ and 4.01 respectively. Therefore, we discard the LJ results and conclude that both the EAM and modified Morse potentials are best suited for this framework. Moving window shock simulations using the new EOS parameters for the EAM potential and Langevin thermostat are presented in Ch. 6.3.

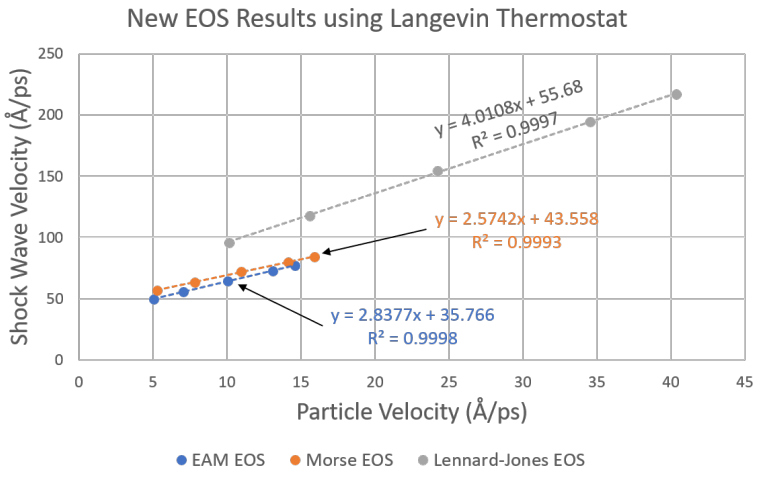

(a)

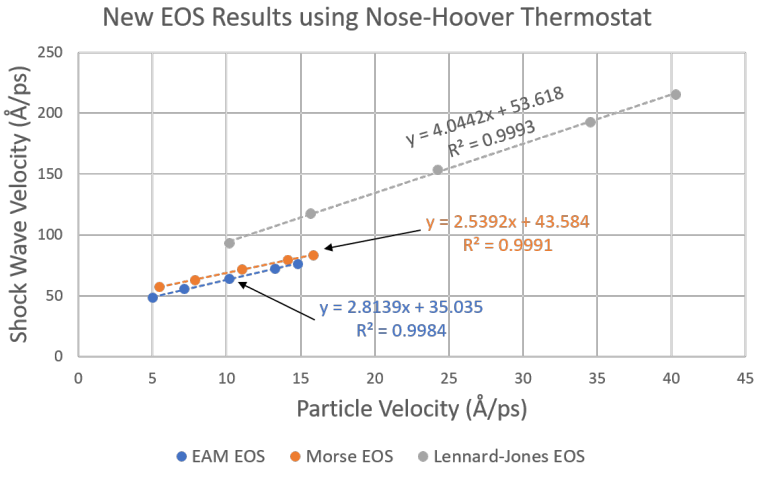

(b)

Figure 6.5: Calculations of the new empirical EOS parameters for all three potentials with (a) Langevin and (b) Nose-Hoover thermostats. The slope of each equation is the new S value and the y-intercept is the new C_0 value.

6.3 Moving window simulations with new EOS

In Fig. 6.6, we present still shots for a propagating shock with an input shock velocity of 50 $\mathring{A}/ps$. This simulation uses the EAM potential with the Langevin thermostat, and we introduce the new EOS parameters derived in Ch. 6.2 into Eq. (2.13). We again utilize a 10,000 atom domain with 100 atoms in each CA region, and we employ periodic boundary conditions as described in Ch. 3.1. As before, we overlay the initial shock wave with its later positions at 100 ps increments and thus show the evolution in time of the shock wave over a period of 1,000 ps. With these simulations, we observe much better agreement between the input shock velocity and simulated shock velocity from the moving window atomistic method. Comparing Fig. 6.6 with Fig. 6.1, it is apparent that when using the new EOS parameters, the midpoint of the shock front maintains its position at the center of the WA region for a much longer time than when using the original EOS parameters. Therefore, the atomistic domain is now properly "following" the propagating shock.

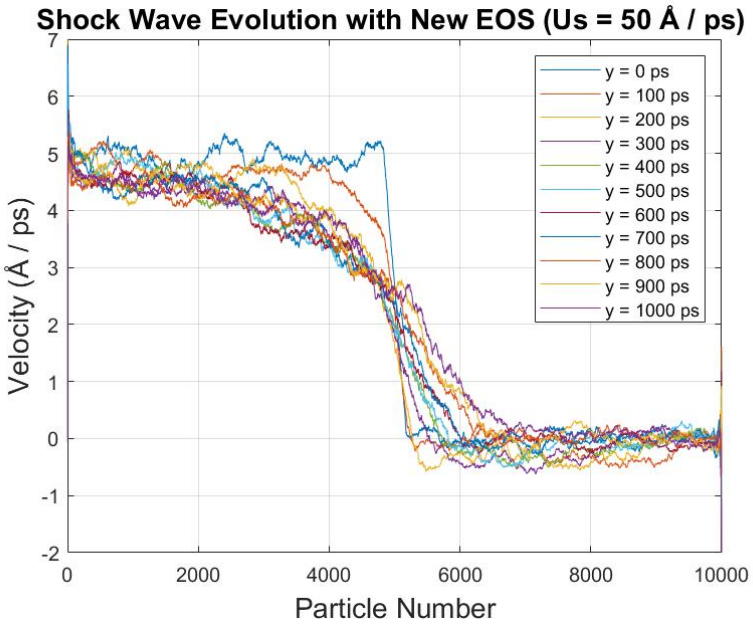

Figure 6.6: Propagation of a shock wave using the EAM potential with the Langevin thermostat and incorporating the new EOS parameters (U_S = 50 $\mathring{A}/ps$).

This increased agreement between the moving window atom replacement frequency and the shock wave frequency can also be represented by plotting the average momentum of the 1D chain vs. time as seen in Fig. 6.7. As before, the solid lines represent the calculated momenta

while the dotted lines represent the linear fits. From Fig. 6.7, we observe that each shock wave initially drifts to the left before either maintaining its position in the center or drifting steadily to the right. Comparing this plot to Fig. 6.3, it is apparent that the slopes of the linear fits for all five shock wave trials have decreased significantly, and thus the average particle velocity of the system is noticeably more constant over time than previously observed. This indicates that the shocks simulated using the new EOS parameters remain relatively stationary in the WA region much longer than the shocks presented in Ch. 6.1. Therefore, the empirical EOS parameters derived in Ch. 6.2 produce shock speeds which closely match their corresponding input shock speed (U_S). We are thus able to model steady state shock wave propagation through the atomistic framework for a protracted amount of time.

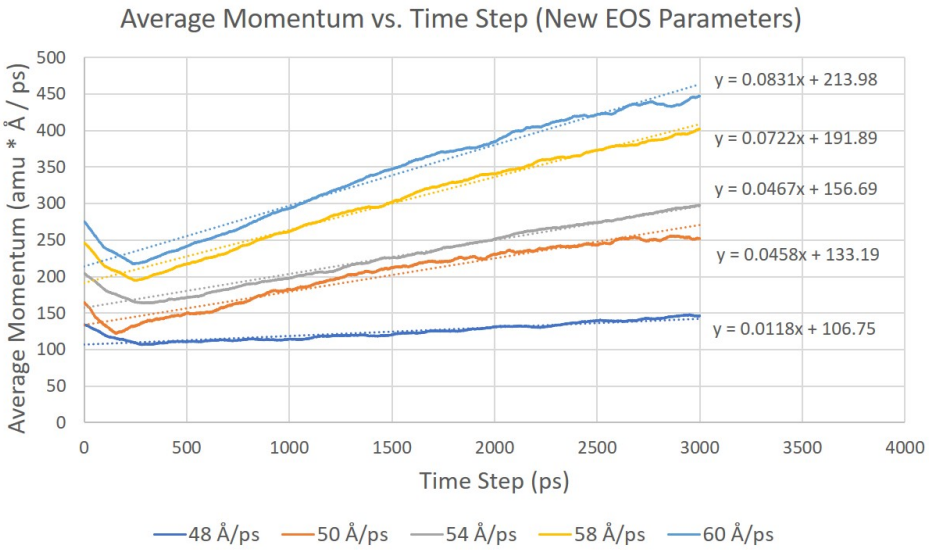

Figure 6.7: Average momentum vs. time of the entire domain for various input shock velocities using the EAM potential and Langevin thermostat. These simulations were produced using the EOS parameters derived in Ch. 6.2.

For each of these shock wave simulations, we do observe an increase in the shock thickness over time. This effect is evident in Fig. 6.6. Although the midpoint of the shock front remains relatively stationary, the shock "spreads out" across the WA region at higher time steps. This is a consequence of the shock developing a structure as it propagates. A structured shock wave is a well-established and characterized phenomenon [95]. As such, care must be taken to ensure that the WA region is sufficiently large to account for the entire structured shock. Otherwise, the shock wave could potentially 'leak' out of the WA region and start impinging on the WA/CA

interfaces. To understand this phenomenon further, we increase the domain size of the WA region and perform additional shock simulations with the new EOS parameters. These results are presented in Ch. 6.4.

6.4 Effect of domain size

As we saw in Ch. 6.3, the shock wave was developing a structure and exhibiting a length scale. In [95], Chhabildas and Assay calculate an upper limit of $3.0\ ns$ and a lower limit of $0.03\ ns$ for the shock rise time (RT_S) in Cu. Using the new EOS, we perform shock simulations using the following shock input velocities: $48, 50, 54, 58$, and $60\ \mathring{A}/ps$. Assuming the upper limit of $3.0\ ns$ for the shock rise time as well as the highest shock wave velocity of $60\ \mathring{A}/ps$, we can obtain a maximum value for the shock thickness (T_S) as follows:

$$T_S = U_S \times RT_S = 60\mathring{A}/ps \times 3,000ps = 180,000\mathring{A} \tag{6.2}$$

Since our previous framework contained only 10,000 atoms with an equilibrium spacing of $2.556\ \mathring{A}$ between atoms, the domain may not have been large enough to allow the shock to completely equilibrate. Hence, we increase the domain size to 80,000 atoms ($\sim 204,500\ \mathring{A}$) and perform shock simulations with the new EOS. Results for input shock velocities of 50 and $60\ \mathring{A}/ps$ respectively can be seen in Fig. 6.8.

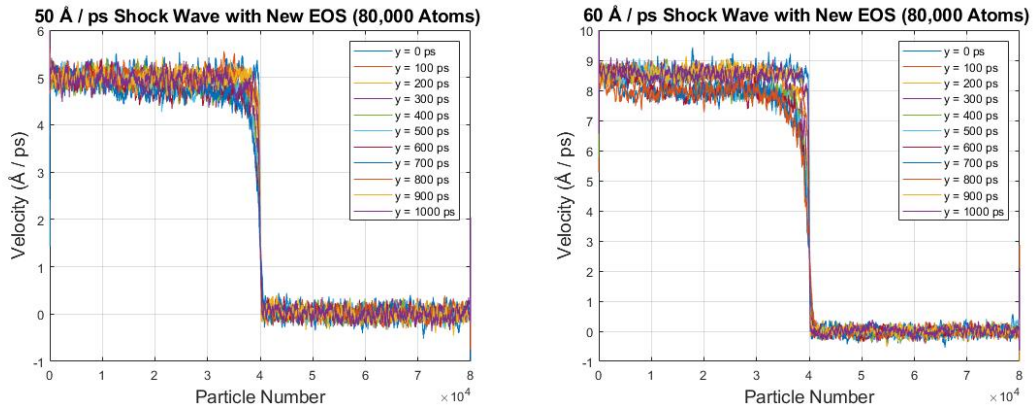

(a) (b)

Figure 6.8: Propagation of the SWF using the EAM potential with the Langevin thermostat for input shock velocities of *50* and *60* $\mathring{A}/ps$. The atomistic domain contains 80,000 total atoms.

For both shock wave trials, we clearly observe the shock wave maintaining its position at the center of the WA region over time. We can also see the efficacy of the moving window in Fig. 6.9. Here, we plot the average momentum of the 80,000 atom domain vs. time for the first 2 ns. It can be observed that the average momentum stabilizes within $750 - 1000\ ps$ for all the shock speeds. This is when the shock is achieving a structure. After the initial stabilization period, the shock achieves steady state with the moving window adding and removing atoms at regular intervals. A very slow decline in average momentum is observed after the initial stabilization period. This damping is attributed to the numerical errors in the algorithm and second-order errors in the new equation of state. Further corrections to the equation of state as well as a reduction in the time step for the integration algorithm should reduce this slow damping.

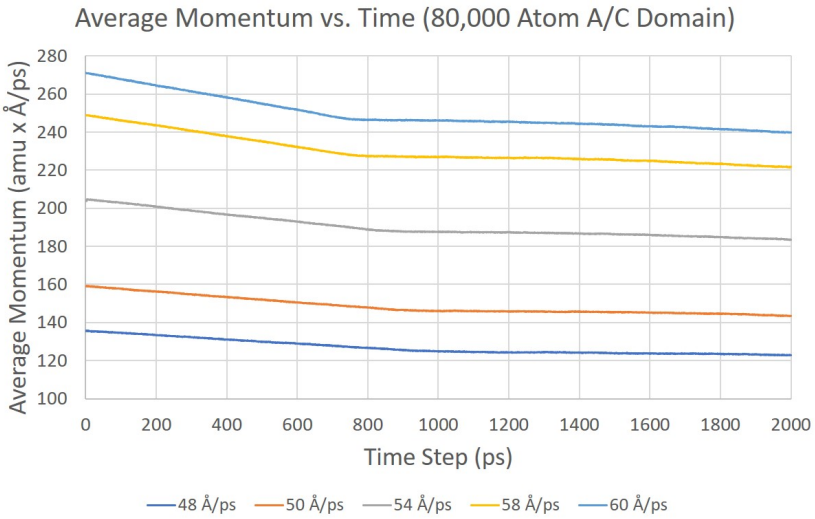

Figure 6.9: Average momentum vs. time of the entire domain for five different input shock velocities using the EAM potential and Langevin thermostat. The domain contains 80,000 total atoms.

Chapter 7

Conclusion

The propagation of shock waves in homogeneous solids has been extensively studied [2]. Shock waves typically occur in materials subjected to high strain rate loading conditions, and the shock response of a material at any length scale is inextricably linked to its response at lower length scales. Shock response of materials has been modeled since the early 70s using purely atomistic methods, but such methods suffer from domain boundary effects and unrealistic strain rates [1]. Concurrent multiscale methods have been developed since the early 90s in which the domain is divided into a coarse-scaled (continuum) region and a fine-scaled (atomistic) region. While such schemes have been successful in modeling material defects and their motion, they have not been extended to model shock propagation through materials. To model shock wave propagation using concurrent multiscale methods, the atomistic domain must move along with the shock wave.

In this paper, we developed a one-dimensional moving window atomistic framework to model long-time steady state shock wave propagation. The framework is composed of a window region governed by classic MD equations containing the shock wave. This is flanked by boundary regions governed by continuum shock states. The motion of the window region is achieved by adding/removing atoms from/to the boundary region to/from the window region. In Chs. 2 and 3, we introduced the one-dimensional formulation and a classic single wave Riemann problem as well as implemented two thermostats and three potentials into the framework. We introduced the moving window formulation and presented a detailed explanation of this scheme in Ch. 4.

In Ch. 5, we performed three sets of studies to verify the implementation of the thermostats, potential functions, and A/C interfaces respectively. First, in Ch. 5.1, we verified that the Langevin and Nose-Hoover thermostats preserved the system at a constant temperature (canonical NVT ensemble). We observed that regardless of the potential function used, both thermostats maintained the system at the mean input temperature for the entire run-time of 3,000 ps. Next, in Ch. 5.2, we verified that the three potential functions could accurately represent mechanical properties of the 1D framework. This was accomplished by computing the tangent modulus using the LJ and Morse potentials and computing the bulk modulus using the EAM potential. Both the LJ and Morse potentials produced accurate tangent moduli for temperatures ranging from 0 - 450 K, and the EAM potential produced an accurate cohesive energy and bulk modulus at 0 K. Finally, in Ch. 5.3, we verified that there was smooth information transfer between the outer continuum atoms and inner window atoms. We observed that regardless of the thermostat used, all three potentials maintained the entire domain at the mean input particle velocity, and the system did not produce any large traveling waves for the entire run time of 3,000 ps. From these results, we concluded that our atomistic framework was properly implemented.

In Ch. 6, we used the moving window framework to study steady state shock wave propagation in copper. The state of the unshocked material was chosen to be unstressed, at rest, and at room temperature. Using an experimentally observed linear law, jump equations, and a prescribed shock velocity, the state of the shocked material was obtained. It was observed that even with the prescribed window speed being equal to the chosen shock speed, the actual shock contained within the window region nevertheless drifted. Next, we used the framework to obtain corrections to the linear law in a one-dimensional setting. These corrections were then used to obtain a new equation of state and new continuum states for the boundary regions. Finally, large-domain simulations were conducted to ensure that the entire shock width was contained within the window region. It was observed that the framework was successful in capturing long-time steady state motion of the shock wave.

It should be emphasized that this work is not truly atomistic/continuum due to the absence of a classical continuum region with finite element type mesh points. Rather, it serves as a proof

of concept of a movng window technique that can be extended to a classic concurrent multiscale scheme in three dimensions. Additionally, it provides evidence for the ability of the moving window atomistic framework to simulate propagating shock waves. More work is needed to understand the efficacy of this type of MD shock wave modeling in higher dimensions. Such a multi-dimensional framework could be used to study shock wave scattering and microstructural changes upon a shock's interaction with an interface. Finally, this work also demonstrates the ability to use such a framework to obtain shock kinetic relations.

References

[1] M. A. Meyers, *Dynamic behavior of materials*. John wiley & sons, 1994.

[2] L. Davison, *Fundamentals of shock wave propagation in solids*. Springer Science & Business Media, 2008.

[3] M. Rice, R. G. McQueen, and J. Walsh, "Compression of solids by strong shock waves," in *Solid state physics*, vol. 6, pp. 1–63, Elsevier, 1958.

[4] G. Duvall and G. Fowles, "High pressure physics and chemistry," *Academic Press, New York*, pp. 209–223, 1963.

[5] D. Doran and R. Linde, "Solid state physics, vol. 19," 1966.

[6] W. Murri, D. Curran, C. Peterson, and R. Crewdson, "Advances in high pressure research," 1974.

[7] L. Davison and R. A. Graham, "Shock compression of solids," *Physics Reports*, vol. 55, no. 4, pp. 255–379, 1979.

[8] R. A. Graham, *Solids under high-pressure shock compression: mechanics, physics, and chemistry*. Springer Science & Business Media, 2012.

[9] G. T. (Rusty) Gray, "High-Strain-Rate Deformation: Mechanical Behavior and Deformation Substructures Induced," *Annual Review of Materials Research*, vol. 42, no. 1, pp. 285–303, 2012.

[10] S. J. Fensin, J. P. Escobedo, G. T. Gray, B. M. Patterson, C. P. Trujillo, and E. K. Cerreta, "Dynamic damage nucleation and evolution in multiphase materials," *Journal of Applied Physics*, vol. 115, no. 20, 2014.

[11] J. F. Bingert, R. M. Suter, J. Lind, S. F. Li, R. Pokharel, and C. P. Trujillo, "High-Energy Diffraction Microscopy Characterization of Spall Damage," pp. 397–403, 2014.

[12] A. Paskin and G. Dienes, "Molecular dynamic simulations of shock waves in a three-dimensional solid," *Journal of Applied Physics*, vol. 43, no. 4, pp. 1605–1610, 1972.

[13] A. Parskin and G. Dienes, "A model for shock waves in solids and evidence for a thermal catastrophe," *Solid State Communications*, vol. 17, no. 2, pp. 197–200, 1975.

[14] A. Paskin, A. Gohar, and G. Dienes, "Simulations of shock waves in solids," *Journal of Physics C: Solid State Physics*, vol. 10, no. 19, p. L563, 1977.

[15] A. Paskin, A. Gohar, and G. Dienes, "Simulations of shock waves in solids," *Journal of Physics and Chemistry of Solids*, vol. 39, no. 12, pp. 1307–1311, 1978.

[16] D. Tsai and R. MacDonald, "Second sound in a solid under shock compression," *Journal of Physics C: Solid State Physics*, vol. 6, no. 8, p. L171, 1973.

[17] D. H. Tsai and R. A. MacDonald, "Heat pulse propagation in a crystal: A molecular dynamical calculation," *Solid State Communications*, vol. 14, no. 11, pp. 1269–1273, 1974.

[18] D. Tsai and R. MacDonald, "Molecular-dynamical study of second sound in a solid excited by a strong heat pulse," *Physical Review B*, vol. 14, no. 10, p. 4714, 1976.

[19] D. Tsai and R. MacDonald, "Shock wave profile in a crystalline solid," *Journal of Physics C: Solid State Physics*, vol. 11, no. 9, p. L365, 1978.

[20] R. J. Hardy, "Formulas for determining local properties in molecular-dynamics simulations: Shock waves," *The Journal of Chemical Physics*, vol. 76, no. 1, pp. 622–628, 1982.

[21] J. Irving and J. G. Kirkwood, "The statistical mechanical theory of transport processes. iv. the equations of hydrodynamics," *The Journal of chemical physics*, vol. 18, no. 6, pp. 817–829, 1950.

[22] E. M. Bringa, J. U. Cazamias, P. Erhart, J. Stölken, N. Tanushev, B. D. Wirth, R. E. Rudd, and M. J. Caturla, "Atomistic shock Hugoniot simulation of single-crystal copper," *Journal of Applied Physics*, vol. 96, pp. 3793–3799, oct 2004.

[23] S. G. Srinivasan, M. I. Baskes, and G. J. Wagner, "Atomistic simulations of shock induced microstructural evolution and spallation in single crystal nickel," *Journal of Applied Physics*, vol. 101, no. 4, 2007.

[24] G. E. Norman, A. Y. Kuksin, V. V. Stegailov, A. V. Yanilkin, M. Elert, M. D. Furnish, R. Chau, N. Holmes, and J. Nguyen, "Atomistic simulation of plasticity and fracture of crystalline and polycrystalline metals under high strain rate," in *AIP conference Proceedings*, vol. 955, pp. 329–334, 2008.

[25] S. J. Fensin, J. P. Escobedo-Diaz, C. Brandl, E. K. Cerreta, G. T. Gray, T. C. Germann, and S. M. Valone, "Effect of loading direction on grain boundary failure under shock loading," *Acta Materialia*, vol. 64, pp. 113–122, 2014.

[26] D. R. Tramontina, E. N. Hahn, M. A. Meyers, and E. M. Bringa, "Simulation of tantalum nanocrystals under shock-wave loading: Dislocations and twinning," in *AIP Conference Proceedings 1793*, p. 070002, 2017.

[27] A. Higginbotham, M. J. Suggit, E. M. Bringa, P. Erhart, J. A. Hawreliak, G. Mogni, N. Park, B. A. Remington, and J. S. Wark, "Molecular dynamics simulations of shock-induced deformation twinning of a body-centered-cubic metal," *Physical Review B*, vol. 88, p. 104105, sep 2013.

[28] S. J. Fensin, S. M. Valone, E. K. Cerreta, J. P. Escobedo-Diaz, G. T. Gray, K. Kang, and J. Wang, "Effect of grain boundary structure on plastic deformation during shock

compression using molecular dynamics," *Modelling and Simulation in Materials Science and Engineering*, vol. 21, no. 1, 2013.

[29] E. J. Reed, L. E. Fried, and J. D. Joannopoulos, "A Method for Tractable Dynamical Studies of Single and Double Shock Compression," *Physical Review Letters*, vol. 90, no. 23, p. 235503, 2003.

[30] E. B. Tadmor and R. E. Miller, *Modeling materials: continuum, atomistic and multiscale techniques*. Cambridge University Press, 2011.

[31] J. Fan, *Multiscale analysis of deformation and failure of materials*, vol. 5. John Wiley & Sons, 2011.

[32] S. Xu, L. Xiong, Q. Deng, and D. L. McDowell, "Mesh refinement schemes for the concurrent atomistic-continuum method," *International Journal of Solids and Structures*, vol. 90, pp. 144–152, 2016.

[33] S. Kohlhoff, P. Gumbsch, and H. Fischmeister, "Crack propagation in bcc crystals studied with a combined finite-element and atomistic model," *Philosophical Magazine A*, vol. 64, no. 4, pp. 851–878, 1991.

[34] W. A. Curtin and R. E. Miller, "Atomistic/continuum coupling in computational materials science," *Modelling and simulation in materials science and engineering*, vol. 11, no. 3, p. R33, 2003.

[35] H. S. Park and W. K. Liu, "An introduction and tutorial on multiple-scale analysis in solids," *Computer methods in applied mechanics and engineering*, vol. 193, no. 17-20, pp. 1733–1772, 2004.

[36] X. Li and E. Weinan, "Multiscale modeling of the dynamics of solids at finite temperature," *Journal of the Mechanics and Physics of Solids*, vol. 53, no. 7, pp. 1650–1685, 2005.

[37] H. S. Park, E. G. Karpov, W. K. Liu, and P. A. Klein, "The bridging scale for two-dimensional atomistic/continuum coupling," *Philosophical Magazine*, vol. 85, no. 1, pp. 79–113, 2005.

[38] D. L. McDowell, "A perspective on trends in multiscale plasticity," *International Journal of Plasticity*, vol. 26, no. 9, pp. 1280–1309, 2010.

[39] Y. Chen, J. Zimmerman, A. Krivtsov, and D. L. McDowell, "Assessment of atomistic coarse-graining methods," *International Journal of Engineering Science*, vol. 49, no. 12, pp. 1337–1349, 2011.

[40] D. W. Brenner, "Challenges to marrying atomic and continuum modeling of materials," *Current Opinion in Solid State and Materials Science*, vol. 17, no. 6, pp. 257–262, 2013.

[41] R. E. Miller and E. B. Tadmor, "A unified framework and performance benchmark of fourteen multiscale atomistic/continuum coupling methods," *Modelling and simulation in materials science and engineering*, vol. 17, no. 5, p. 053001, 2009.

[42] S. Xu and X. Chen, "Modeling dislocations and heat conduction in crystalline materials: atomistic/continuum coupling approaches," *International Materials Reviews*, pp. 1–32, 2018.

[43] E. Saether, V. Yamakov, and E. H. Glaessgen, "An embedded statistical method for coupling molecular dynamics and finite element analyses," *International journal for numerical methods in engineering*, vol. 78, no. 11, pp. 1292–1319, 2009.

[44] W. Cai, M. de Koning, V. V. Bulatov, and S. Yip, "Minimizing boundary reflections in coupled-domain simulations," *Physical Review Letters*, vol. 85, no. 15, p. 3213, 2000.

[45] E. Weinan and Z. Huang, "Matching conditions in atomistic-continuum modeling of materials," *Physical Review Letters*, vol. 87, no. 13, p. 135501, 2001.

[46] S. Qu, V. Shastry, W. Curtin, and R. E. Miller, "A finite-temperature dynamic coupled atomistic/discrete dislocation method," *Modelling and simulation in materials science and engineering*, vol. 13, no. 7, p. 1101, 2005.

[47] S. B. Ramisetti, G. Anciaux, and J.-F. Molinari, "Spatial filters for bridging molecular dynamics with finite elements at finite temperatures," *Computer Methods in Applied Mechanics and Engineering*, vol. 253, pp. 28–38, 2013.

[48] J. Knap and M. Ortiz, "An analysis of the quasicontinuum method," *Journal of the Mechanics and Physics of Solids*, vol. 49, no. 9, pp. 1899–1923, 2001.

[49] Y. Kulkarni, J. Knap, and M. Ortiz, "A variational approach to coarse graining of equilibrium and non-equilibrium atomistic description at finite temperature," *Journal of the Mechanics and Physics of Solids*, vol. 56, no. 4, pp. 1417–1449, 2008.

[50] J. S. Amelang, G. N. Venturini, and D. M. Kochmann, "Summation rules for a fully nonlocal energy-based quasicontinuum method," *Journal of the Mechanics and Physics of Solids*, vol. 82, pp. 378–413, 2015.

[51] W. Kim, M. Luskin, D. Perez, A. Voter, and E. Tadmor, "Hyper-QC: An accelerated finite-temperature quasicontinuum method using hyperdynamics," *Journal of the Mechanics and Physics of Solids*, vol. 63, pp. 94–112, feb 2014.

[52] L. E. Shilkrot, R. E. Miller, and W. A. Curtin, "Coupled Atomistic and Discrete Dislocation Plasticity," *Physical Review Letters*, vol. 89, p. 025501, jun 2002.

[53] G. Anciaux, T. Junge, M. Hodapp, J. Cho, J.-F. Molinari, and W. Curtin, "The Coupled Atomistic/Discrete-Dislocation method in 3d part I: Concept and algorithms," *Journal of the Mechanics and Physics of Solids*, vol. 118, pp. 152–171, sep 2018.

[54] M. Hodapp, G. Anciaux, J.-F. Molinari, and W. Curtin, "Coupled atomistic/discrete dislocation method in 3D Part II: Validation of the method," *Journal of the Mechanics and Physics of Solids*, vol. 119, pp. 1–19, oct 2018.

[55] J. Cho, J.-F. Molinari, W. A. Curtin, and G. Anciaux, "The coupled atomistic/discrete-dislocation method in 3d. Part III: Dynamics of hybrid dislocations," *Journal of the Mechanics and Physics of Solids*, vol. 118, pp. 1–14, sep 2018.

[56] V. V. Zhakhovskii, K. Nishihara, and S. I. Anisimov, "Shock wave structure in dense gases," *Journal of Experimental and Theoretical Physics Letters*, vol. 66, pp. 99–105, Jul 1997.

[57] V. V. Zhakhovsky, M. M. Budzevich, N. A. Inogamov, I. I. Oleynik, and C. T. White, "Two-zone elastic-plastic single shock waves in solids," *Physical review letters*, vol. 107, no. 13, p. 135502, 2011.

[58] S. P. Marsh, *LASL shock Hugoniot data*, vol. 5. Univ of California Press, 1980.

[59] A. L. Ruoff, "Linear shock-velocity-particle-velocity relationship," *Journal of Applied Physics*, vol. 38, no. 13, pp. 4976–4980, 1967.

[60] R. McQueen, S. Marsh, J. Taylor, J. Fritz, and W. Carter, "The equation of state of solids from shock wave studies," *High velocity impact phenomena*, vol. 293, pp. 294–417, 1970.

[61] R. Jeanloz, "Shock wave equation of state and finite strain theory," *Journal of Geophysical Research: Solid Earth*, vol. 94, no. B5, pp. 5873–5886, 1989.

[62] J. R. Asay and M. Shahinpoor, *High-pressure shock compression of solids*. Springer Science & Business Media, 2012.

[63] J. Knowles, "On the relation between particle velocity and shock wave speed for thermoelastic materials," *Shock Waves*, vol. 12, no. 2, pp. 137–144, 2002.

[64] R. Abeyaratne and J. K. Knowles, "Kinetic relations and the propagation of phase boundaries in solids," *Archive for rational mechanics and analysis*, vol. 114, no. 2, pp. 119–154, 1991.

[65] R. Abeyaratne and J. K. Knowles, "On the propagation of maximally dissipative phase boundaries in solids," *Quarterly of applied mathematics*, vol. 50, no. 1, pp. 149–172, 1992.

[66] V. Agrawal and K. Bhattacharya, "Shock wave propagation through a model one dimensional heterogeneous medium," *International Journal of Solids and Structures*, vol. 51, no. 21-22, pp. 3604–3618, 2014.

[67] G. I. Kerley, "The linear us-up relation in shock-wave physics," *arXiv preprint arXiv:1306.6916*, 2013.

[68] W. C. Swope, H. C. Andersen, P. H. Berens, and K. R. Wilson, "A computer simulation method for the calculation of equilibrium constants for the formation of physical clusters of molecules: Application to small water clusters," *The Journal of Chemical Physics*, vol. 76, no. 1, pp. 637–649, 1982.

[69] J. E. Jones, "On the determination of molecular fields.—ii. from the equation of state of a gas," *Proceedings of the Royal Society of London. Series A, Containing Papers of a Mathematical and Physical Character*, vol. 106, no. 738, pp. 463–477, 1924.

[70] L. Verlet, "Computer" experiments" on classical fluids. i. thermodynamical properties of lennard-jones molecules," *Physical review*, vol. 159, no. 1, p. 98, 1967.

[71] J. Lv, M. Bai, W. Cui, and X. Li, "The molecular dynamic simulation on impact and friction characters of nanofluids with many nanoparticles system," *Nanoscale research letters*, vol. 6, no. 1, p. 200, 2011.

[72] R. A. MacDonald and W. M. MacDonald, "Thermodynamic properties of fcc metals at high temperatures," *Physical review B*, vol. 24, no. 4, p. 1715, 1981.

[73] M. Wen, S. Whalen, R. S. Elliott, and E. B. Tadmor, "Interpolation effects in tabulated interatomic potentials," *Modelling and Simulation in Materials Science and Engineering*, vol. 23, no. 7, p. 074008, 2015.

[74] S. Foiles, M. Baskes, and M. S. Daw, "Embedded-atom-method functions for the fcc metals cu, ag, au, ni, pd, pt, and their alloys," *Physical review B*, vol. 33, no. 12, p. 7983, 1986.

[75] M. S. Daw and M. I. Baskes, "Embedded-atom method: Derivation and application to impurities, surfaces, and other defects in metals," *Physical Review B*, vol. 29, no. 12, p. 6443, 1984.

[76] M. S. Daw, S. M. Foiles, and M. I. Baskes, "The embedded-atom method: a review of theory and applications," *Materials Science Reports*, vol. 9, no. 7-8, pp. 251–310, 1993.

[77] Y. Mishin, M. Mehl, D. Papaconstantopoulos, A. Voter, and J. Kress, "Structural stability and lattice defects in copper: Ab initio, tight-binding, and embedded-atom calculations," *Physical Review B*, vol. 63, no. 22, p. 224106, 2001.

[78] S. Lepri, R. Livi, and A. Politi, "Thermal conduction in classical low-dimensional lattices," *Physics reports*, vol. 377, no. 1, pp. 1–80, 2003.

[79] W. K. Liu, E. Karpov, S. Zhang, and H. Park, "An introduction to computational nanomechanics and materials," *Computer methods in applied mechanics and engineering*, vol. 193, no. 17-20, pp. 1529–1578, 2004.

[80] K. Binder, J. Horbach, W. Kob, W. Paul, and F. Varnik, "Molecular dynamics simulations," *Journal of Physics: Condensed Matter*, vol. 16, no. 5, p. S429, 2004.

[81] W. G. Hoover, K. Aoki, C. G. Hoover, and S. V. De Groot, "Time-reversible deterministic thermostats," *Physica D: Nonlinear Phenomena*, vol. 187, no. 1-4, pp. 253–267, 2004.

[82] K. Jolley and S. P. Gill, "Modelling transient heat conduction in solids at multiple length and time scales: A coupled non-equilibrium molecular dynamics/continuum approach," *Journal of Computational Physics*, vol. 228, no. 19, pp. 7412–7425, 2009.

[83] T. Schneider and E. Stoll, "Molecular-dynamics study of a three-dimensional one-component model for distortive phase transitions," *Physical Review B*, vol. 17, no. 3, p. 1302, 1978.

[84] S. Gill, Z. Jia, B. Leimkuhler, and A. Cocks, "Rapid thermal equilibration in coarse-grained molecular dynamics," *Physical Review B*, vol. 73, no. 18, p. 184304, 2006.

[85] S. Nose, "Constant-temperature molecular dynamics," *Journal of Physics: Condensed Matter*, vol. 2, no. S, p. SA115, 1990.

[86] J. W. Gibbs, *Elementary principles in statistical mechanics*. Courier Corporation, 2014.

[87] D. Squire, A. Holt, and W. Hoover, "Isothermal elastic constants for argon. theory and monte carlo calculations," *Physica*, vol. 42, no. 3, pp. 388–397, 1969.

[88] J. Lutsko, "Generalized expressions for the calculation of elastic constants by computer simulation," *Journal of applied physics*, vol. 65, no. 8, pp. 2991–2997, 1989.

[89] F. Bavaud, P. Choquard, and J.-R. Fontaine, "Statistical mechanics of elastic moduli," *Journal of statistical physics*, vol. 42, no. 3-4, pp. 621–646, 1986.

[90] J. R. Ray, M. C. Moody, and A. Rahman, "Calculation of elastic constants using isothermal molecular dynamics," *Physical Review B*, vol. 33, no. 2, p. 895, 1986.

[91] J. R. Ray, "Elastic constants and statistical ensembles in molecular dynamics," *Computer physics reports*, vol. 8, no. 3, pp. 109–151, 1988.

[92] G. Gao, K. Van Workum, J. D. Schall, and J. A. Harrison, "Elastic constants of diamond from molecular dynamics simulations," *Journal of Physics: Condensed Matter*, vol. 18, no. 32, p. S1737, 2006.

[93] W. Cai, J. Li, and S. Yip, "1.09 molecular dynamics," *Compr. Nucl. Mater., edited by JMK Rudy (Elsevier, Oxford, 2012)*, pp. 249–265, 2012.

[94] W. A. Curtin and R. E. Miller, "A perspective on atomistic-continuum multiscale modeling," *Modelling and Simulation in Materials Science and Engineering*, vol. 25, no. 7, p. 071004, 2017.

[95] L. C. Chhabildas and J. R. Asay, "Rise-time measurements of shock transitions in aluminum, copper, and steel," *Journal of Applied Physics*, vol. 50, no. 4, pp. 2749–2756, 1979.